A&A, 711, A34 (2026)
https://doi.org/10.1051/0004-6361/202554937
© The Authors 2026

Astronomy & Astrophysics
Special issue

Euclid Quick Data Release (Q1)

Euclid Quick Data Release (Q1)

XXXIV. First detections from the *Euclid* galaxy cluster workflow

Euclid Collaboration: S. Bhargava[1,⋆], C. Benoist[1], A. H. Gonzalez[2], M. Maturi[3,4], J.-B. Melin[5], S. A. Stanford[6], E. Munari[7,8], M. Vannier[1], C. Murray[9], S. Maurogordato[1], A. Biviano[7,8], J. Macias-Perez[10], J. G. Bartlett[9], F. Pacaud[11], A. Widmer[9], M. Meneghetti[12,13], B. Sartoris[14,7], M. Aguena[7], G. Alguero[10], S. Andreon[15], S. Bardelli[12], L. Baumont[16,7,8], M. Bolzonella[12], R. Cabanac[17], A. Cappi[12,1], G. Castignani[12], C. Combet[10], J. Comparat[18], S. Farrens[19], Z. Ghaffari[7,8], P. A. Giles[20], C. Giocoli[12,13], M. Girardi[16,7], N. A. Hatch[21], L. Ingoglia[22], A. Iovino[15], G. A. Mamon[23,24], S. Mei[9,25], L. Moscardini[26,12,13], S. Mourre[1,27], J. Odier[10], G. W. Pratt[19], P. Tarrío[28], G. Toni[26,12,4], J. Weller[14,18], E. Zucca[12], N. Aghanim[29], B. Altieri[30], A. Amara[31], N. Auricchio[12], C. Baccigalupi[8,7,32,33], M. Baldi[34,12,13], A. Balestra[35], P. Battaglia[12], F. Bellagamba[34,12], A. Bonchi[36], E. Branchini[37,38,15], M. Brescia[39,40], J. Brinchmann[41,42], S. Camera[43,44,45], V. Capobianco[45], C. Carbone[46], J. Carretero[47,48], S. Casas[49], M. Castellano[50], S. Cavuoti[40,51], K. C. Chambers[52], A. Cimatti[53], C. Colodro-Conde[54], G. Congedo[55], C. J. Conselice[56], L. Conversi[57,30], Y. Copin[58], F. Courbin[59,60], H. M. Courtois[61], M. Cropper[62], A. Da Silva[63,64], H. Degaudenzi[65], G. De Lucia[7], A. M. Di Giorgio[66], C. Dolding[62], H. Dole[29], F. Dubath[65], C. A. J. Duncan[56], X. Dupac[30], S. Dusini[67], A. Ealet[58], S. Escoffier[68], M. Farina[66], R. Farinelli[12], F. Faustini[50,36], S. Ferriol[58], F. Finelli[12,69], P. Fosalba[70,71], S. Fotopoulou[72], M. Frailis[7], E. Franceschi[12], M. Fumana[46], S. Galeotta[7], K. George[14], B. Gillis[55], P. Gómez-Alvarez[73,30], J. Gracia-Carpio[18], B. R. Granett[15], A. Grazian[35], F. Grupp[18,14], L. Guzzo[74,15,75], S. Gwyn[76], S. V. H. Haugan[77], J. Hoar[30], H. Hoekstra[78], W. Holmes[79], F. Hormuth[80], A. Hornstrup[81,82], P. Hudelot[23], S. Ilić[83,17], K. Jahnke[84], M. Jhabvala[85], B. Joachimi[86], E. Keihänen[87], S. Kermiche[68], A. Kiessling[79], M. Kilbinger[19], B. Kubik[58], K. Kuijken[78], M. Kümmel[14], M. Kunz[88], H. Kurki-Suonio[89,90], Q. Le Boulc'h[91], A. M. C. Le Brun[92], D. Le Mignant[93], P. Liebing[62], S. Ligori[45], P. B. Lilje[77], V. Lindholm[89,90], I. Lloro[94], G. Mainetti[91], D. Maino[74,46,75], E. Maiorano[12], O. Mansutti[7], S. Marcin[95], O. Marggraf[11], M. Martinelli[50,96], N. Martinet[93], F. Marulli[26,12,13], R. Massey[97], E. Medinaceli[12], M. Melchior[98], Y. Mellier[24,23], E. Merlin[50], G. Meylan[99], A. Mora[100], M. Moresco[26,12], R. Nakajima[11], C. Neissner[101,48], R. C. Nichol[31], S.-M. Niemi[102], J. W. Nightingale[103], C. Padilla[101], S. Paltani[65], F. Pasian[7], K. Pedersen[104], W. J. Percival[105,106,107], V. Pettorino[102], S. Pires[19], G. Polenta[36], M. Poncet[108], L. A. Popa[109], L. Pozzetti[12], F. Raison[18], R. Rebolo[54,110,111], A. Renzi[112,67], J. Rhodes[79], G. Riccio[40], E. Romelli[7], M. Roncarelli[12], R. Saglia[14,18], Z. Sakr[3,17,113], A. G. Sánchez[18], D. Sapone[114], J. A. Schewtschenko[55], P. Schneider[11], T. Schrabback[115], A. Secroun[68], E. Sefusatti[7,8,32], G. Seidel[84], S. Serrano[70,116,71], P. Simon[11], C. Sirignano[112,67], G. Sirri[13], J. Skottfelt[117], L. Stanco[67], J. Steinwagner[18], P. Tallada-Crespí[47,48], A. N. Taylor[55], I. Tereno[63,118], S. Toft[119,120], R. Toledo-Moreo[121], F. Torradeflot[48,47], I. Tutusaus[17], L. Valenziano[12,69], J. Valiviita[89,90], T. Vassallo[14,7], G. Verdoes Kleijn[122], A. Veropalumbo[15,38,37], Y. Wang[123], A. Zacchei[7,8], G. Zamorani[12], F. M. Zerbi[15], V. Allevato[40], M. Ballardini[124,125,12], E. Bozzo[65], C. Burigana[22,69], P. Casenove[108], D. Di Ferdinando[13], J. A. Escartin Vigo[18], G. Fabbian[126], L. Gabarra[127], J. Martín-Fleitas[100], S. Matthew[55], N. Mauri[53,13], R. B. Metcalf[26,12], A. Pezzotta[128,18], M. Pöntinen[89], C. Porciani[11], I. Risso[129], V. Scottez[24,130], M. Sereno[12,13], M. Tenti[13], M. Viel[8,7,33,32,131], M. Wiesmann[77], Y. Akrami[132,133], I. T. Andika[134,135], S. Anselmi[67,112,136], M. Archidiacono[74,75], F. Atrio-Barandela[137], K. Benson[62], P. Bergamini[74,12], D. Bertacca[112,35,67], M. Bethermin[138], A. Blanchard[17], L. Blot[139,136], H. Böhringer[18,140,141], S. Borgani[16,8,7,32,131], M. L. Brown[56], S. Bruton[142], A. Calabro[50], B. Camacho Quevedo[70,71], F. Caro[50], C. S. Carvalho[118], T. Castro[7,32,8,131], Y. Charles[93], F. Cogato[26,12], A. R. Cooray[143], M. Costanzi[16,7,8], O. Cucciati[12], S. Davini[38], F. De Paolis[144,145,146], G. Desprez[122], A. Díaz-Sánchez[147], J. J. Diaz[148], S. Di Domizio[37,38], J. M. Diego[149], P. Dimauro[50,150], P.-A. Duc[138], A. Enia[34,12], Y. Fang[14], A. G. Ferrari[13], P. G. Ferreira[127], A. Finoguenov[89], A. Fontana[50], A. Franco[145,144,146], K. Ganga[9], J. García-Bellido[132], T. Gasparetto[7], E. Gaztanaga[71,70,151], F. Giacomini[13], F. Gianotti[12], G. Gozaliasl[152,89], M. Guidi[34,12], C. M. Gutierrez[153], A. Hall[55], W. G. Hartley[65], C. Hernández-Monteagudo[111,54], H. Hildebrandt[154], J. Hjorth[104],

⋆ Corresponding author: sunayana.bhargava@oca.eu

Open Access article, published by EDP Sciences, under the terms of the Creative Commons Attribution License (https://creativecommons.org/licenses/by/4.0), which permits unrestricted use, distribution, and reproduction in any medium, provided the original work is properly cited.
This article is published in open access under the Subscribe to Open model. Subscribe to A&A to support open access publication.

J. J. E. Kajava[155,156], Y. Kang[65], V. Kansal[157,158], D. Karagiannis[124,159], K. Kiiveri[87], C. C. Kirkpatrick[87], S. Kruk[30], J. Le Graet[68], L. Legrand[160,161], M. Lembo[124,125], F. Lepori[162], G. Leroy[163,97], G. F. Lesci[26,12], J. Lesgourgues[49], L. Leuzzi[26,12], T. I. Liaudat[164], S. J. Liu[66], A. Loureiro[165,166], G. Maggio[7], M. Magliocchetti[66], E. A. Magnier[52], F. Mannucci[167], R. Maoli[168,50], C. J. A. P. Martins[169,41], L. Maurin[29], M. Migliaccio[170,171], M. Miluzio[30,172], P. Monaco[16,7,32,8], A. Montoro[71,70], C. Moretti[33,131,7,8,32], G. Morgante[12], K. Naidoo[151], A. Navarro-Alsina[11], S. Nesseris[132], F. Passalacqua[112,67], K. Paterson[84], L. Patrizii[13], A. Pisani[68,173], D. Potter[162], S. Quai[26,12], M. Radovich[35], P.-F. Rocci[29], P. Rosati[124,12], S. Sacquegna[144,145,146], M. Sahlén[174], D. B. Sanders[52], E. Sarpa[33,131,32], J. Schaye[78], A. Schneider[162], M. Schultheis[1], D. Sciotti[50,96], E. Sellentin[175,78], L. C. Smith[176], K. Tanidis[127], G. Testera[38], R. Teyssier[173], S. Tosi[37,38,15], A. Troja[112,67], M. Tucci[65], C. Valieri[13], A. Venhola[177], D. Vergani[12], G. Verza[178], P. Vielzeuf[68], N. A. Walton[176], E. Soubrie[29], and D. Scott[179]

(Affiliations can be found after the references)

Received 1 April 2025 / Accepted 27 July 2025

ABSTRACT

The first survey data release by the *Euclid* mission covers approximately 63 deg^2 in the Euclid Deep Fields to the same depth as the Euclid Wide Survey. This paper showcases, for the first time, the performance of cluster finders on *Euclid* data and presents examples of validated clusters in the Quick Release 1 (Q1) imaging data. We identify clusters using two algorithms (`AMICO` and `PZWav`) implemented in the *Euclid* cluster-detection pipeline. We explore the internal consistency of detections from the two codes, and cross-match detections with known clusters from other surveys using external multi-wavelength and spectroscopic data sets. This enables assessment of the *Euclid* photometric redshift accuracy and also of systematics such as mis-centring between the optical cluster centre and centres based on X-ray and/or Sunyaev–Zeldovich observations. We report 426 joint `PZWav` and `AMICO`-detected clusters with high signal-to-noise ratios over the full Q1 area in the redshift range $0.2 \leq z \leq 1.5$. The chosen redshift and signal-to-noise thresholds are motivated by the photometric quality of the early *Euclid* data. We provide richness estimates for each of the *Euclid*-detected clusters and show its correlation with various external cluster mass proxies. Due to the limited area and evolving data quality, the sample is not intended to serve as a reference for cosmological applications, but to verify and validate the cluster workflow. Out of the full sample, 77 systems are potentially new to the literature. Overall, the Q1 cluster catalogue demonstrates a successful validation of the workflow ahead of the *Euclid* Data Release 1, based on the consistency of internal and external properties of *Euclid*-detected clusters.

Key words. surveys – galaxies: clusters: general – large-scale structure of Universe

1. Introduction

The European Space Agency (ESA) *Euclid* mission is designed to map the geometry of the Universe in unprecedented detail using optical and near-infrared wide-field imaging and spectroscopy; the completed survey will cover 14 000 deg^2 of the extragalactic sky, observing over 1.5 billion galaxies out to a redshift $z \approx 2$ (Euclid Collaboration: Mellier et al. 2025). Furthermore, *Euclid* is expected to detect and characterise approximately 10^5 galaxy clusters and groups (Sartoris et al. 2016; Euclid Collaboration: Adam et al. 2019), driving a tremendous leap in cosmological constraints from joint cluster abundance, clustering, and weak lensing mass estimates (e.g., Maturi et al. 2019, Lesci et al. 2022, Abbott et al. 2020, Costanzi et al. 2021, Romanello et al. 2025).

This paper presents a validation of the *Euclid* galaxy cluster workflow on the *Euclid* Quick Release 1 (Q1) data set (Euclid Quick Release Q1 2025), constituting the first survey data released by the mission (Euclid Collaboration: Aussel et al. 2026). The data consists of three non-contiguous fields that cover approximately 63 deg^2 – one in the northern and two in the southern hemisphere. We detect clusters and characterise candidates with high signal-to-noise ratio (S/N) across the three fields, favouring a conservative approach during this early phase of *Euclid* data.

Numerous simulation-based evaluations have been conducted on the accuracy of recovering *Euclid* cluster masses (e.g. Euclid Collaboration: Ingoglia et al. 2025; Euclid Collaboration: Giocoli et al. 2024), as well as multi-wavelength cluster observables Euclid Collaboration: Ragagnin et al. (2025). Moreover, extensive tests of the cluster workflow have been performed on the Flagship simulation (Euclid Collaboration: Castander et al. 2025) to better understand the *Euclid* selection function for clusters (Cabanac et al., in prep.). This paper explores the impact of galaxy selection and quality cuts on the cluster workflow's ability to robustly detect and characterise galaxy clusters on real *Euclid* data for the first time.

We examine the distribution in S/N, optical richness and redshift for our cluster detections. In addition, cluster redshift estimates are compared to external photometric and spectroscopic data. We utilised the extensive multi-wavelength coverage at near-infrared, optical, millimetre, and X-ray wavelengths of the Q1 fields in the literature to identify counterparts of the *Euclid* detections. We evaluate centring offset distributions and study the properties of missed objects.

Despite the limited area of the Q1 data release, *Euclid*'s high galaxy density allows us to perform a detailed characterisation of the first clusters detected by the *Euclid* mission. This provides a secure training ground for the *Euclid* Data Release 1 (DR1), which will cover approximately 1900 deg^2 and form the basis of the first cosmological analysis.

The paper outline is as follows. In Sect. 2 we describe the input galaxy selection performed on the *Euclid* source catalogues and associated masks. In Sect. 3 we describe the two cluster detection algorithms implemented in the mission Science Ground Segment (SGS), and we detail the construction of the combined cluster catalogue. Sect. 4 presents cross-matches to external cluster catalogues. In Sect. 5 we describe spectroscopic validation of the Q1 cluster catalogue using ground-based spectroscopic surveys. We explore the scientific return of this

first validation of *Euclid* clusters and the outlook for the future in Sect. 6. Unless otherwise stated, we adopt a flat ΛCDM model following Planck Collaboration VI (2020), with $H_0 = 67.4\,\mathrm{km\,s^{-1}\,Mpc^{-1}}$ and $\Omega_\mathrm{m} = 0.315$.

2. Input data

2.1. The three Euclid Q1 patches

The Q1 release consists of three non-contiguous fields that, upon completion of the survey, will constitute the Euclid Deep Survey (EDS), as described in Euclid Collaboration: Mellier et al. (2025). Although the purpose of these fields is to gain approximately two magnitudes in depth compared to the Euclid Wide Survery (EWS), the Q1 fields have been imaged to the nominal EWS depth for this first data release.

The Q1 survey area comprises the Euclid Deep Field North (EDF-N), the Euclid Deep Field South (EDF-S), and the Euclid Deep Field Fornax (EDF-F), covering a total area of 63 deg^2. Based on the galaxy catalogues used in this analysis, the total area for each field is reported in Fig. 1. The EDF-N is an approximately 23 deg^2 circular field located at the northern ecliptic pole. The EDF-F is a 12 deg^2 circular field including the Chandra Deep Field South (CDF-S), which has numerous ground- and space-based ancillary observations (as described in Sect. 4). Lastly, the EDF-S is a 28 deg^2 field with an extended shape that encompasses two adjacent deep-drilling fields of the Vera C. Rubin Legacy Survey of Space and Time (LSST). The exact spatial distribution of the fields is illustrated in Figure 1 of the Q1 overview paper, Euclid Collaboration: Aussel et al. (2026).

The effective area, average photometric redshift scatter and bias corresponding to these fields are computed based on the selection criteria used for cluster detection (see Sect. 2.2) and the external photometric bands available for each of the three fields. The latter are: The Ultraviolet Near Infrared Optical Northern Survey[1] (UNIONS, Gwyn et al. 2025), Dark Energy Camera (DECAM)[2], described in Abbott et al. (2021), and Hyper-Suprime Cam (HSC)[3], described in Aihara et al. (2022).

2.2. The galaxy selection

Galaxy selection in the Q1 fields is primarily based on the information provided by the OU-MER and OU-LE3 Organisational Units (OU) of the *Euclid* SGS. We refer the reader to Euclid Collaboration: Aussel et al. (2026) for a detailed description the input products. Detailed descriptions of the VIS and NISP instruments can be found in Euclid Collaboration: Cropper et al. (2025) and Euclid Collaboration: Jahnke et al. (2025), respectively. The sources used in our analysis satisfy the following criteria.

- They are detected in the VIS image (`VIS_DET` = 1). This choice is motivated by the presence of persistence in the NISP detector that is not yet fully solved. This effect currently prevents us from using sources detected in the NISP images only, and therefore limits our cluster search to redshifts lower than the nominal redshift $z = 2$. This restriction will be lifted in future releases.
- They are covered by images in all bands used in the considered sky patch (`FLUX_*_2FWHM_APER` ≠ `NaN`).
- They are not saturated (`Flag_*` ≠ 3).
- They are not classified as stars at the 99% confidence level (`POINT_LIKE_PROB` ≤ 0.95).
- They are not within stellar polygons designed to mask regions around bright stars and their diffraction spikes in the VIS and stacked NIR images (`DET_QUALITY_FLAG[bits 7 and 8]` = 0).
- They are not located in `HEALPix`[4] (Górski et al. 2005; Zonca et al. 2019) pixels of the inter-band (*Euclid* VIS + NIR and external bands) COVERAGE map where the pixel coverage is below 80%.
- They are limited to an H_E magnitude of 24[5] to ensure galaxy completeness and homogeneous data quality. At these magnitudes the average signal to noise expected for H_E-band photometry is ∼5 (Euclid Collaboration: Enia et al. 2026).

A more detailed description of the individual flags used in the galaxy selection can be found in Euclid Collaboration: Romelli et al. (2026). In addition to these criteria, three sets of additional masks are applied: larger circular masks around bright stars to reject areas that are spoiled by image artefacts in the ground-based images; elliptical masks to cover bright galaxies in the foreground; and masks around extended stellar systems. The last two sets of masks are derived from the masking performed by the DR10 Legacy Survey[6].

The normalised galaxy number counts as a function of H_E magnitude for the three Q1 patches are presented in Fig. 1. The galaxy selection leads to consistent number counts that reach a maximum at a H_E magnitude of 24, justifying our choice in limiting magnitude.

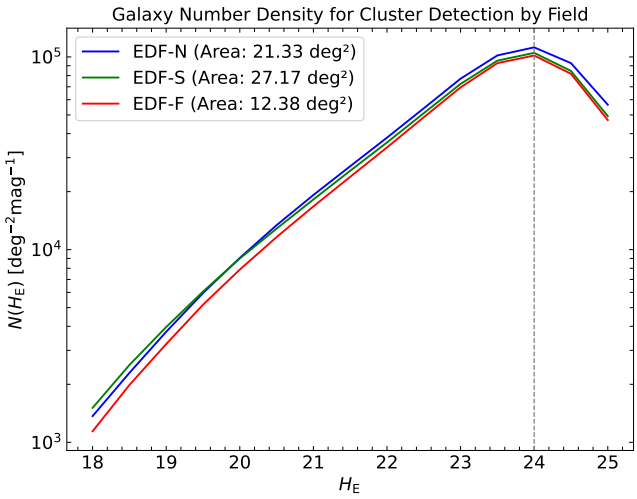

Fig. 1. Galaxy number densities for the three *Euclid* Q1 patches after applying the filtering described in Sect. 2.2. The number densities are binned as a function of magnitude in the *Euclid* NIR-H_E band, as well as by the effective area. The dashed vertical line indicates a magnitude cut of $H_\mathrm{E} < 24$ in the galaxy selection.

[1] https://www.skysurvey.cc
[2] https://noirlab.edu/public/programs/ctio/victor-blanco-4m-telescope/decam/
[3] https://subarutelescope.org/en/subaru2/instrument/hsc/
[4] http://healpix.sourceforge.net
[5] Corresponding to `FLUX_H_UNIF` > 0.912 and obtained from $H_\mathrm{E} = -2.5\log_{10}$ `FLUX_H_UNIF`[μJy] − 23.9.
[6] https://www.legacysurvey.org/dr10/external

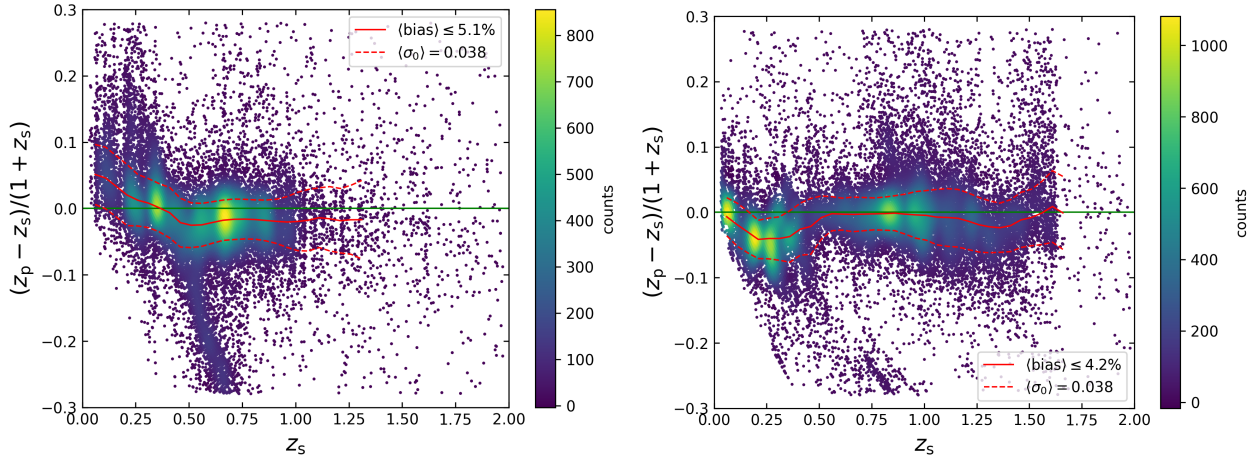

Fig. 2. Residuals of the median photometric redshift relative to the spectroscopic redshift for 25 416 galaxies in the EDF-F field (left) and 36 564 galaxies in the EDF-N (right). The spectroscopic information comes from a compilation of publicly available external spectroscopic surveys, starting from a redshift of $z_s = 0.05$ in the two figures. The red lines indicate the associated bias and scatter, estimated in redshift bins containing at least 200 galaxies.

2.3. Photometric redshifts

High-quality photometric redshifts (photo-z) are an essential ingredient for both cluster detection and richness estimation. The photo-z are derived with the template-fitting code `Phosphoros`, whose application to the *Euclid* data is detailed in Euclid Collaboration: Tucci et al. (2026). Here, we evaluate the photo-z quality for galaxies used in our cluster studies. In particular, we assess the consistency of the computed redshift probability distribution (PDZ) by comparison to a set of 26 964 publicly available galaxy spectroscopic redshifts in the EDF-F and 38 950 in the EDF-N. The number of available redshifts for the EDF-S is considerably lower (of order 100 s). Details of the external spectroscopic data set matched to Q1 can be found in Section 5.2 and Table 5 of Euclid Collaboration: Tucci et al. (2026).

In Fig. 2, we compare the median values of the PDZ to the associated spectroscopic redshift. Statistical errors are computed in the redshift range from 0.05 to 1.5 where most of the spectroscopic data is concentrated. Defining the normalised offset $X = (z_p - z_s)/(1 + z_s)$, where z_p is the PDZ median value and z_s is the spectroscopic value, a relatively stable mean scatter of $\sigma_0 \approx 0.04$ and a residual bias of $\pm 2.5\%$ ($\pm 4.1\%$) can be observed for the EDF-F (EDF-N). We do not make this comparison for the EDF-S due to the aforementioned much lower number of objects with external spectroscopic counterparts; however, we expect a similar behaviour to EDF-F due to the same external band coverage.

In this study, PDZs are also critical to associate errors to the photometric redshift measurements, which, in turn, are used to weight galaxies in the cluster detection algorithms presented in Sect. 3.1. To evaluate how well the shape of the PDZs reflect the 'true' photometric redshift errors, we compute the average width of the 15th-to-85th percentiles around the median and compare it to the average offset of the PDZ median value with its associated spectroscopic redshift, where available. This test is performed in photometric redshift bins from $z_p = 0.2$ to 2 which corresponds to the *Euclid* nominal range for cluster searches. The result is shown in Fig. 3. On average, the evolution of the PDZ width with the median photometric redshift is in good agreement with the z_p, z_s scatter. However, the PDZ widths are systematically narrower than expected across the entire redshift range by about 65% for the EDF-N and 15% for the EDF-F field. The underestimation of photo-z uncertainties, particularly in extreme cases with an effective $\sigma_z < 0.01$, can lead to undesired spurious detections if not addressed adequately. To mitigate this issue, we tested two different approaches in the detection algorithms, discussed in Sect. 3.1.

As explained in Euclid Collaboration: Tucci et al. (2026), efforts are ongoing to address the need for photometric bias corrections and the treatment of underestimation of photo-z errors. For a more detailed discussion of the photometric validation, the reader is referred to Sect. 5.2 in the aforementioned paper.

3. Methodology

3.1. Cluster detection

The two cluster detection algorithms used in the *Euclid* galaxy cluster workflow, `AMICO` (see Sect. 3.1.1) and `PZWav` (see Sect. 3.1.2), were selected through a series of cluster-finding challenges (Euclid Collaboration: Adam et al. 2019). These two algorithms employ complementary approaches to cluster detection. `AMICO` is a linear optimal matched-filter code that uses prior knowledge of the properties of the cluster galaxy population for cluster identification; `PZWav` favours a more model-independent approach, making minimal assumptions about cluster properties by using only positions and photometric redshift data.

Within the Q1 framework, the algorithms analyse sky regions known as cluster tiles, consisting of an ensemble of sky tile catalogues and maskes produced by the SGS OU-MER pipeline. The MER tiles themselves are defined geometrically and have a size of approximately $0.^{\circ}25 \times 0.^{\circ}25$ (Euclid Collaboration: Romelli et al. 2026). Each MER tile has an associated source catalogue and coverage mask that incorporates the features detailed in Sect. 2.2. After running on a cluster tile (one for each of the three fields), the two cluster algorithms produce individual catalogues with a list containing the angular positions, redshift, and S/N of all detected sources.

3.1.1. `AMICO`

We briefly describe the main features of `AMICO` (Adaptive Matched Identifier of Clustered Objects), with more details

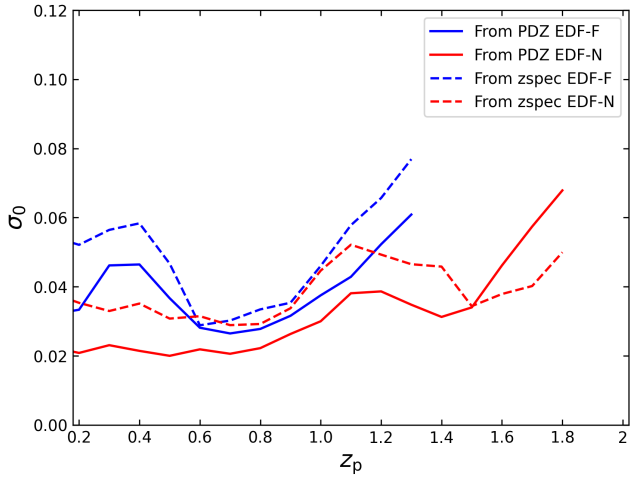

Fig. 3. Average scatter of the photometric redshifts in bins of photometric redshift, derived from the comparison to spectroscopic redshifts (dashed lines) or from the mean width of 15th-to-85th percentiles around the median of the individual PDZ (solid lines) for the same subset of galaxies. The lines stop when fewer than 200 galaxies are available in the considered redshift bin.

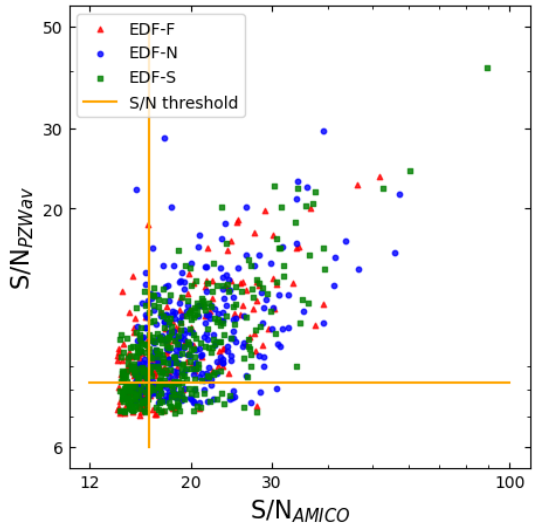

Fig. 4. Comparison of the S/N of the matched AMICO and PZWav detections. The yellow lines indicate the adopted S/N thresholds that ensure 15 detections per square degree by both algorithms in the redshift range $0.2 \leq z \leq 1.5$. The precise S/N thresholds are stated in Sect. 3.2.

available in Bellagamba et al. (2018) and Maturi et al. (2019). AMICO works with catalogues of galaxy angular positions, magnitudes, and full photometric redshift probabilities, avoiding any explicit selection based on the cluster red sequence. The data are modelled as the sum of the desired cluster contribution and a noise component representing contamination from field galaxies. The cluster filter model includes a Schechter luminosity function (Schechter 1976) and a projected NFW (Navarro et al. 1996) radial profile, while the field galaxy distribution at a certain redshift is approximated from the full galaxy sample, weighted by their redshift probabilities. The filter is optimal in the sense that it minimises variance to estimate the signal amplitude, A, calculated on a three-dimensional grid of positions and redshifts (with a chosen resolution of 0.01 in both angular position, in degrees, and redshift). Clusters are identified as the peaks with the highest S/N, followed by iterative 'cleaning' to remove the contributions of detected clusters, thus reducing blending for refining subsequent detections. This process continues to a minimum S/N, directly linked to the amplitude. For this data set, a regularisation term has been introduced to address galaxies whose photometric redshifts exhibit excessively small uncertainties, indicating potential issues with their redshift estimates. Such galaxies can produce an excess of signal in the AMICO amplitude maps, resulting in potential spurious detections. To avoid this issue, the PDZ of galaxies with photometric redshift uncertainties smaller than $\sigma_z = 0.01(1 + z_{\rm med})$, is modelled as a Gaussian with $\sigma = \sigma_z$ and mode located at $z_{\rm med}$. Here, $z_{\rm med}$ is the median value of the input PDZ. We observed an excess in low redshift detections (below $z \leq 0.6$) prior to the regularisation in AMICO, subsequently obtaining comparable numbers to PZWav. Going forwards for DR1, we plan to implement the same criteria, but with a sigma value modelled as a polynomial function fitted to the data – produced from a new release of the photometric redshift algorithm – rather than a scalar value. A similar procedure will be applied to PZWav.

3.1.2. PZWav

The PZWav detection algorithm applies a difference-of-Gaussians smoothing kernel that is designed to detect overdensities on cluster scales, while minimising the impact of larger scale structures on the detection. The code takes as input the positions and full photometric redshift probability distribution functions, PDZ, for each galaxy and generates a data cube in position and redshift containing this information. We refer the reader to Euclid Collaboration: Adam et al. (2019), Werner et al. (2023), and Thongkham et al. (2024) for more detail on the PZWav algorithm. Of particular relevance for the current work, the standard deviations for inner and outer Gaussians in the kernel are set at 300 kpc and 1.2 Mpc. This choice of scales has been found to effectively remove large-scale structure contributions and isolate clusters in both previous surveys (Thongkham et al. 2024) and tests on the Flagship simulations (Cabanac et al., in preparation). Purity and completeness evaluations of the PZWav algorithm are also performed in these two papers. Moreover, previous cluster detection with PZWav has found no significant sensitivity to the dynamical state of the cluster. The chosen redshift bin size in the search is set to 0.06. The wider redshift binning compared to AMICO, by construction, regularises the contribution of galaxies with an excessively narrow PDZ, which would otherwise degrade the results.

3.2. Building the combined catalogue

The cluster detection algorithms were applied to each of the three Q1 fields. The clusters were selected in the redshift range $0.2 \leq z_p \leq 1.5$, where the lower redshift bound corresponds to the nominal *Euclid* cluster catalogue requirement. We note that the upper redshift limit is lower than the one planned for subsequent data releases ($z_p \leq 2.0$), because photometry and photometric redshift estimation still have to be refined for these newly released data; the upper redshift limit for this sample is set by the poorly constrained behaviour of the *Euclid* photometric redshifts at $z_p \geq 1.5$, as shown in Figs. 2 and 3. In addition, as described in Sect. 2.2, the provisional requirement that all objects in the galaxy catalogues be detected in the VIS instrument necessarily restricts us to lower redshifts than what is anticipated for future data releases. While the principal catalogue is limited to $z \leq 1.5$, we nevertheless explore objects at $z \geq 1.5$ in the joint catalogue

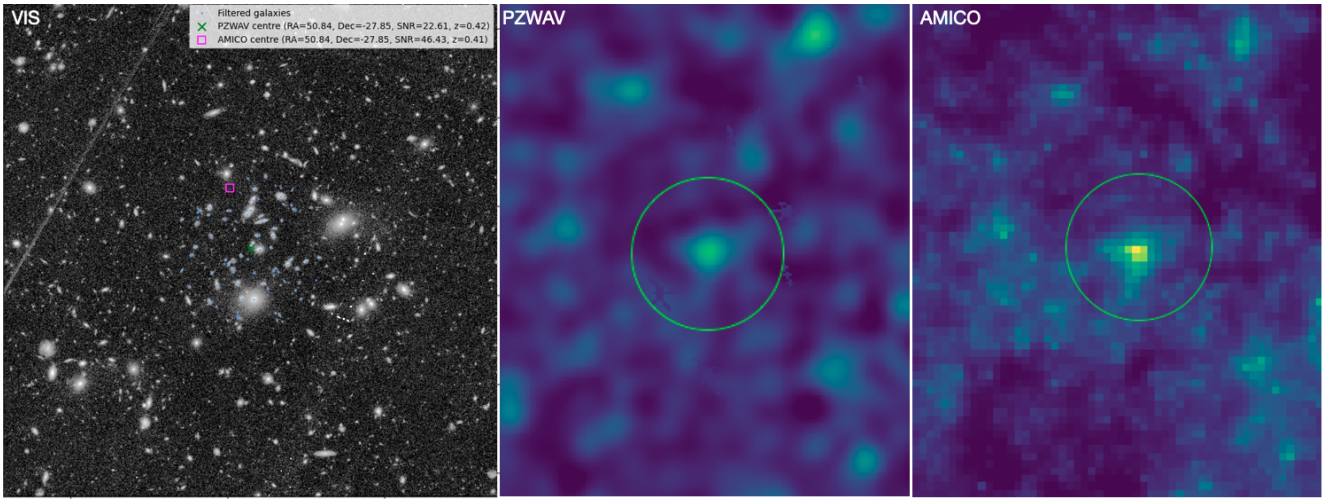

Fig. 5. Left: VIS zoom-in of $2' \times 2'$ at the location of a PZWav and AMICO-detected cluster, at redshift $z_p = 0.42$, located in the EDF-F. The cluster has a *Euclid* richness of $\lambda = 56.1$. The middle and right panels show PZWav and AMICO amplitude maps, respectively centred at the cluster position. The radius of the green circle is 6 arcminutes.

in Sect. 4.7. This extension is undertaken with the knowledge of limitations in redshift accuracy, allowing us to assess the reliability of the cluster detections and highlight the most promising candidates in this regime.

For this initial Q1 analysis, we ensured a consistent number density of detections between the two algorithms by adjusting the minimum S/N accordingly. Specifically, we used thresholds of S/N = 16.1 (16.9) for AMICO and S/N = 8.3 (8.2) for PZWav, to guarantee 15 detections per square degree for each algorithm in the EDF-F and EDF-S (EDF-N). The different S/N thresholds applied to the southern and northern fields is due to the different photometric redshift quality, as discussed in Sect. 2.3. The absolute difference in values adopted for AMICO and PZWav is due to different definitions of the S/N by each finder. The S/N thresholds for each of the three fields were determined by visually inspecting a large number of detections to ensure an initial cluster sample that excludes clearly spurious detections. In the following analysis, we prioritise a joint sample of clusters in common between PZWav and AMICO to mitigate known issues in the input galaxy photometric redshifts. Focusing on the joint, high S/N detections for Q1 allows us to perform an initial internal validation of the cluster workflow, enabling us to identify any key issues that may impact the catalogue and subsequent cluster science applications.

To match the cluster detections between AMICO and PZWav, a physical distance of 1 Mpc was chosen, from which an angular search aperture was computed based on the mean cluster redshift of each pair. We imposed an additional constraint on any redshift difference of $\delta z = 0.1(1 + z)$ to minimise the number of erroneous matches to clusters in projection. If multiple matches were found, the highest S/N target was chosen. Fig. 4 shows the comparison of the S/N of the matched systems. The joint catalogue corresponds to the systems in the upper right part of the figure, which consists in 6.4 (EDF-N), 7.0 (EDF-S) and 7.9 (EDF-F) common detections out of the adopted nominal 15 detections per square degree for each algorithm. More of these detections are matched but were found at S/N lower than our thresholds (upper-left and lower-right quadrants of Fig. 4). The 35 highest S/N detections in the resulting joint catalogue are presented in Table A.1. For each entry, we preserved the positions, redshifts, and S/Ns derived by each detection algorithm, whereas the presented richness is computed at the position of the PZWav centres. Finally, the occurrence of fragmentation associated with the two detection algorithms is shown to be low over the overall mass range for clusters, with a more detailed assessment performed in Euclid Collaboration: Adam et al. (2019).

In Fig. 5, we show an example of a candidate cluster within the *Euclid* VIS image (Euclid Collaboration: McCracken et al. 2026) that is detected in both the PZWav and AMICO density maps. We note that the study of individual detections from the two cluster finders is an important aspect in understanding internal differences in the two algorithms. While the scope of this first paper is to assemble a joint list of reliable cluster detections in the Q1 data set, follow-up analyses of the individual PZWav and AMICO catalogues will be pursued prior to DR1, including the statistics of the matched and unmatched detections. Fig. 6 shows the visualisation of the PZWav- and AMICO-detected clusters with the highest S/N in five redshift intervals from combined VIS and NISP colour postage stamps.

The left panel of Fig. 7 compares the redshifts estimated by the two algorithms for the matched catalogue. The shaded pink region illustrates the $\delta z = 0.1(1 + z)$ matching interval, and we see that the redshift difference between matched objects is well within the interval, reinforcing the validity of the matching procedure. The right panel of Fig. 7 shows the internal consistency in the centring performance of the two algorithms.

Finally, we highlight an example of a strong lens detected in one of the cluster candidates in the EDF-S in Fig. 8, which is located in close proximity to both the PZWav and AMICO detection centres. This lens was initially reported in the catalogue of strongly lensed galaxy systems from the Dark Energy Survey Science Verification and Year 1 Observations in Diehl et al. (2017). We note that, thanks to *Euclid*'s superior resolution, in addition to the central lens there is a clearly visible galaxy-galaxy strong lensing event, to the right of the giant arc, involving a cluster member galaxy and likely the same background system which produces the dominant arc. While it is the cluster halo that is responsible for producing strong lensing features on larger scales, cluster galaxies can themselves act as lenses inside the larger lens. Such lensing features are described in greater detail in Meneghetti et al. (2020).

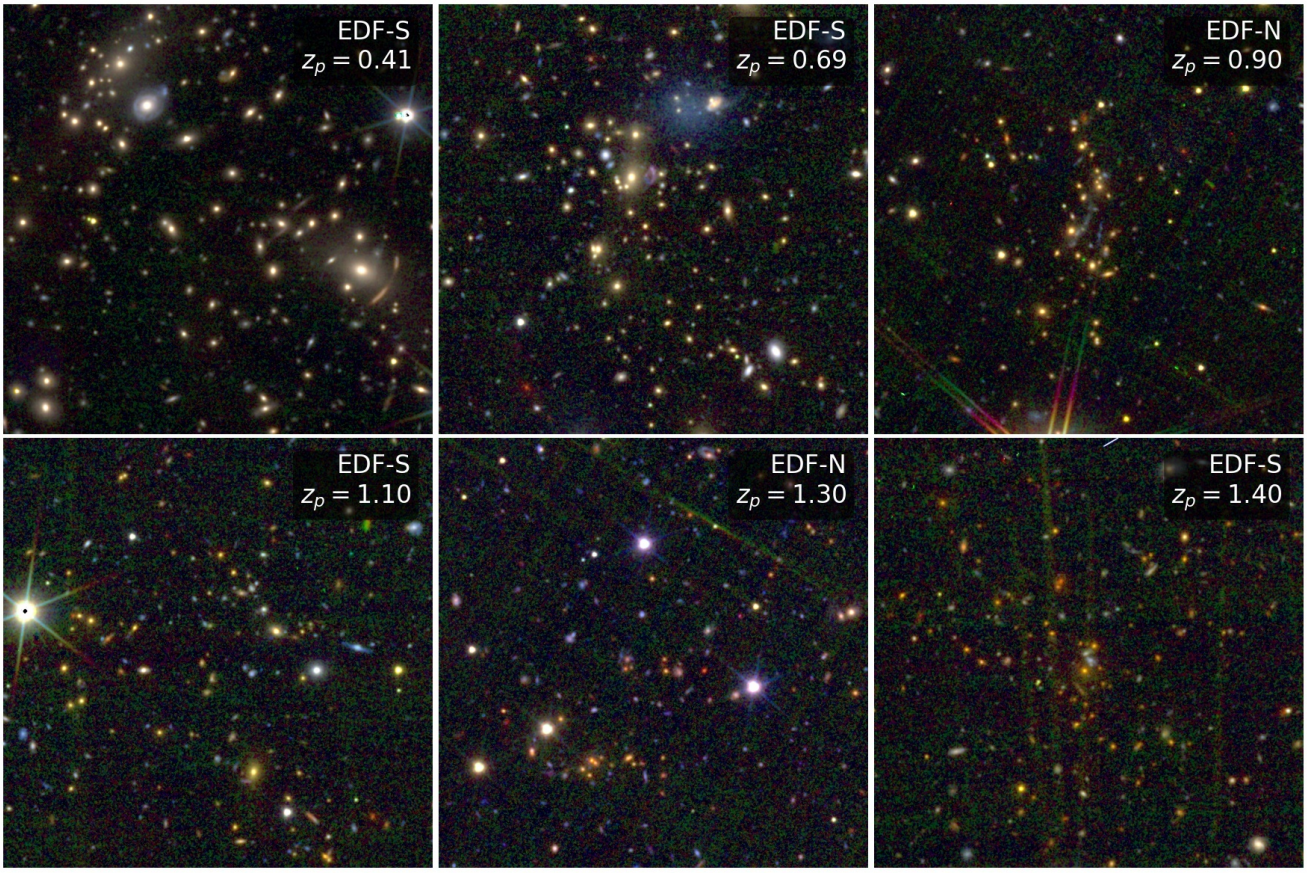

Fig. 6. VIS I_E and NISP Y_E- and H_E-band combined colour postage stamps of $2' \times 2'$ for five of the highest S/N PZWav- and AMICO-detected clusters in six selected redshift intervals ranging from low to high redshift.

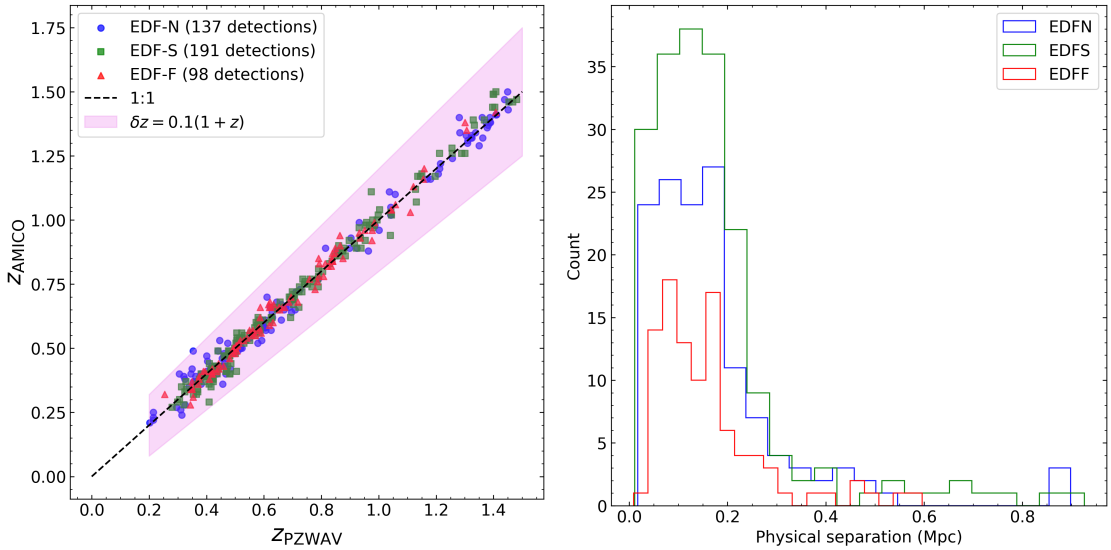

Fig. 7. *Left*: Redshift correlation between the photometric redshift estimate from the cluster finders AMICO and PZWav for all cluster detections in the Q1 region. *Right*: *Euclid*-based centring offset distribution between AMICO and PZWav centres for the catalogues in the three Q1 fields.

Cluster richness is estimated using the SGS LE3 function RICH-CL, which independently employs photometric redshift and red-sequence-based richness assignment derived from the approaches of Castignani & Benoist (2016) and Andreon (2016). Following the prescription of Castignani & Benoist (2016), cluster membership probabilities are computed as a function of galaxy cluster-centric distance, H_E-band magnitude, and photometric redshift. Cluster richness is then calculated as the sum of membership probabilities for members brighter than $H_E^*(z_{cluster}) + 1.5$, where H_E^* is the characteristic magnitude marking the knee of the luminosity function. In this study, $H_E^*(z)$ is estimated from the passive evolution of a burst galaxy with a

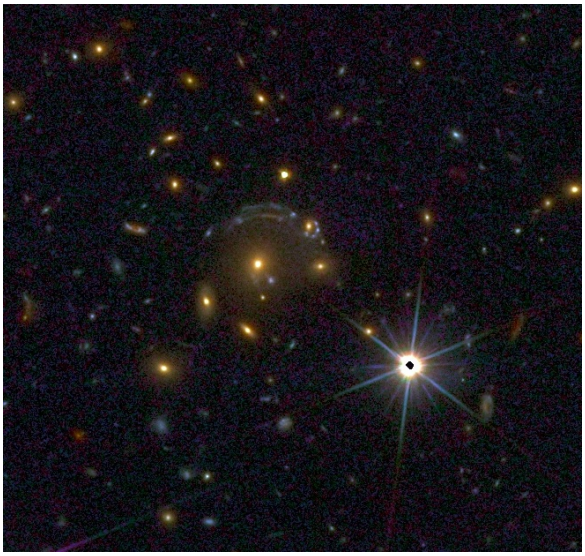

Fig. 8. Zoomed-in image of a strong lens in a PZWav and AMICO-detected cluster at RA = 57.°33, Dec = −48.°96, with a richness $\lambda = 58.7$ and redshift $z_p = 0.58$ in the EDF-S. This cluster is also reported in the catalogue of giant arcs found in the *Euclid* Q1 data release (Euclid Collaboration: Bergamini et al. 2026).

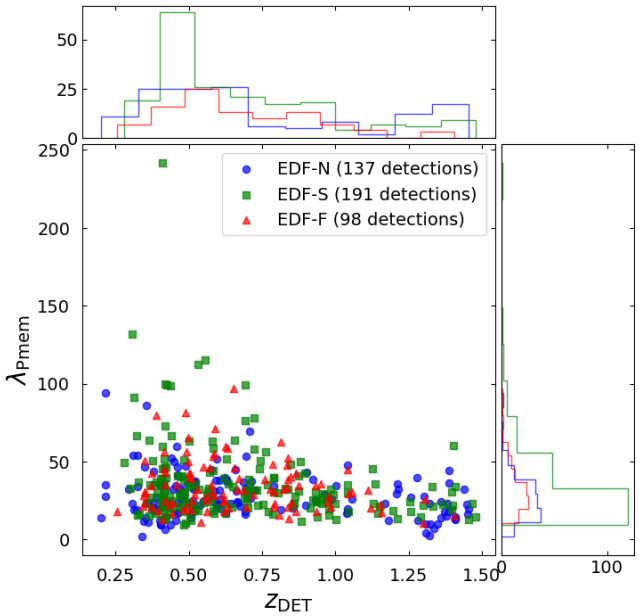

Fig. 9. Combined richness and redshift distributions of the cluster detections across the three fields.

formation redshift $z_{form} = 5$, taken from the PEGASE2 library (burst_sc86_zo.sed, Fioc & Rocca-Volmerange 1997). It is calibrated using the value of $K^\star(z = 0.25)$ derived by Lin et al. (2006) from an observed cluster sample.

We computed the richnesses, λ_{Pmem}, using only the photo-z assignments for this study. We calculate the richness based on the PZWav cluster centre and redshift, but would obtain similar results by using the AMICO centre and redshift, based on the level of positional and redshift agreement shown in the two panels of Fig. 7. The combined richness and redshift distributions are presented in Fig. 9.

We illustrate *Euclid*'s photometric capabilities on the richest cluster detected in the data set, SPT-CLJ0411−4819 in the EDF-S, by showing the $Y_E - H_E$ versus H_E and $I_E - Y_E$ versus Y_E distributions for all galaxies within a distance of 2′ from the cluster position. We observe a clear red sequence in both diagrams, as shown in Fig. 10, left and right panels, respectively.

4. Comparison with external cluster catalogues

4.1. Searching for Euclid counterparts in external data

We cross-correlated the joint Q1 cluster catalogue with external meta-catalogues[7] and individual catalogues. We used meta-catalogues and catalogues primarily selected in X-ray – Meta-Catalogue of X-ray Clusters II (MCXC-II) described in Sadibekova et al. 2024, eROSITA (Bulbul et al. 2024; Kluge et al. 2024) – with the Sunyaev-Zeldovich (SZ) effect – Meta-Catalogue of SZ Clusters (MCSZ) described in Tarrio et al., (in preparation) – and in the optical – Dark Energy Survey (DES) Y1 RedMaPPer (Rykoff et al. 2016; Abbott et al. 2020), and the Abell catalogue (Abell 1958; Abell et al. 1989). We also used the joint X-ray and SZ selected catalogue ComPRASS (Tarrío et al. 2019), the LC[2] (Sereno 2015), and the Meta-Catalogue of Cluster Dispersions (MCCD) described in Euclid Collaboration: Melin et al., (in prep.) for clusters with high-quality velocity dispersion measurements.

We applied the cross-correlation method based on a two-way matching. In brief, for each cluster in the external catalogue (or meta-catalogue), we searched for the closest detection (angular distance on the sky) in the Q1 cluster catalogue. Symmetrically, for each detection in the Q1 catalogue, we searched for the closest cluster in the external catalogue. We then only consider *Euclid* detection-external cluster pairs that are identical in the two directions, hence the name 'two-way matching'.

We then apply additional criteria on the distance d and redshift difference $z_p - z_{external}$ between the detection and the cluster. For the MCXC-II and the MCSZ, we imposed $d < 10'$, $d/\theta_{500} < 2$, and $|z_p - z_{external}| < 3\sigma_{z_p}$, where θ_{500} is the characteristic angular radius of the external cluster[8] and σ_{z_p} is the quoted error on the photometric redshift of the *Euclid* detection. The method is presented in detail in Euclid Collaboration: Melin et al., (in prep.).

In total, we found 4/21/85 counterparts in the external catalogues for the 137/98/191 *Euclid* detections in the EDF-N, EDF-F, and EDF-S fields, respectively. In the EDF-F and the EDF-S, the matches are mainly from RedMaPPer and eROSITA. The EDF-N field is not covered by these two catalogues, which explains the significantly lower number of counterparts that are mainly from the MCXC-II. The total number of detections and matches from the external surveys that fall within the Q1 footprint are listed in Table 1. A detailed breakdown of the individual matches to data sets per Q1 field can be found in Appendix B.

4.2. External photometric redshift comparison

We concentrate on the EDF-S, for which we found the largest number of counterparts, comparing the *Euclid* photometric red-

[7] A meta-catalogue is a combination of different source catalogues with cross-identification of clusters and homogenisation of key quantities, notably redshift and a mass proxy.

[8] $\theta_{500} = R_{500}/D_A$, where R_{500} is the radius within which the average cluster mass M_{500} is 500 times the critical density of the Universe at the cluster's redshift and D_A is the angular diameter distance to the cluster. M_{500} is obtained from the X-ray luminosity for the MCXC-II and from the SZ flux or the SZ S/N for the MCSZ.

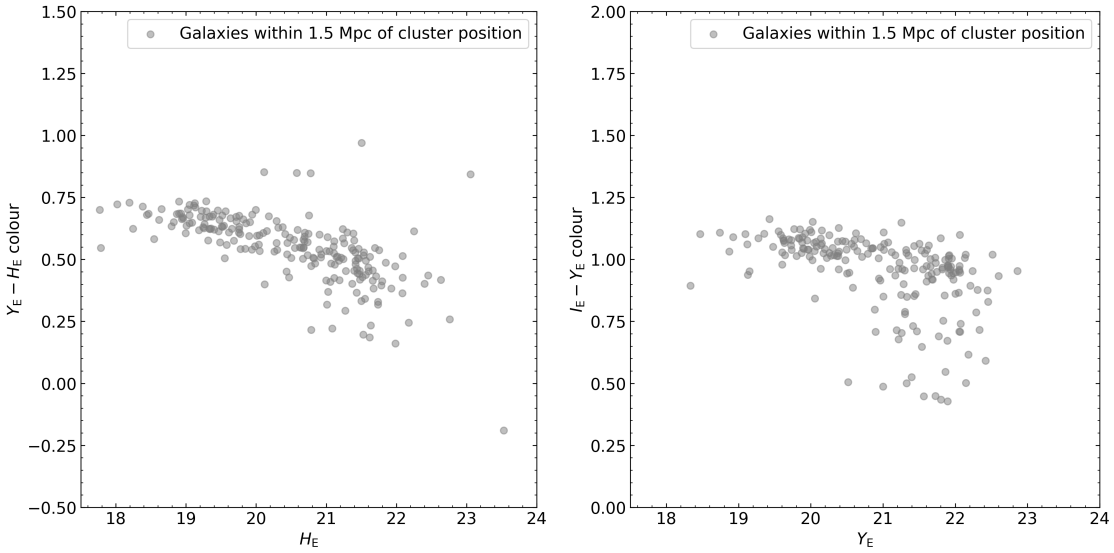

Fig. 10. *Euclid*-only photometry of the galaxy population (grey) located within 1.5 Mpc of the EDF-S cluster position at $z_p = 0.41$ as a function of $Y_E - H_E$ colour and H_E-band magnitude, and $I_E - Y_E$ colour and Y_E-band magnitude (left and right panels, respectively). The cluster shown here, EUCL-Q1-CL J041113.88-481928.2, is the richest in the Q1 catalogue ($\lambda_{Pmem} = 241.5$), also observed by SPT (SPT-CL J0411-4819).

Table 1. Comparison of external data sets with total objects in Q1 footprint and total matches.

Q1 field	No. of *Euclid* cluster detections	No. of clusters found in external data sets	No. of unmatched *Euclid* detections
EDF-N	137	80 (4)	57
EDF-F	98	93 (21)	5
EDF-S	191	176 (85)	15

Notes. The number of *Euclid* detections, matched and unmatched systems correspond to those within the redshift range $0.2 \leq z_p \leq 1.5$. The total number of matches includes the results from the individual catalogues and meta-catalogues, supplementary MaDCoWS2 and WH24 catalogues, and a NED database search (see Sect. 4.6), while the numbers in brackets denote the number of matches using the aforementioned individual catalogues and meta-catalogues only.

shifts with the external cluster redshifts. Only six external redshifts are spectroscopic, so the majority are photometric redshifts. Figure 11 demonstrates that the cluster photometric redshifts have a scatter of around $0.05(1 + z)$ relative to the redshifts (mostly photometric) provided for these clusters by other surveys. At $z < 0.3$ the redshifts also appear to be systematically higher than those from the other surveys. If we restrict ourselves to clusters with $z > 0.3$, the scatter reduces to around $0.03(1 + z)$. We note that a limitation of the current pipeline is that the photometric redshift uncertainties produced by both `PZWav` and `AMICO` are overestimated. Comparing to the scatter relative to the other surveys suggests an overestimation of the *Euclid* cluster photometric redshift uncertainties in Q1 of the order of a factor of 1.7 (2.9 for `AMICO`). The origin of this discrepancy, likely related to the current photo-z PDZ, is still under investigation.

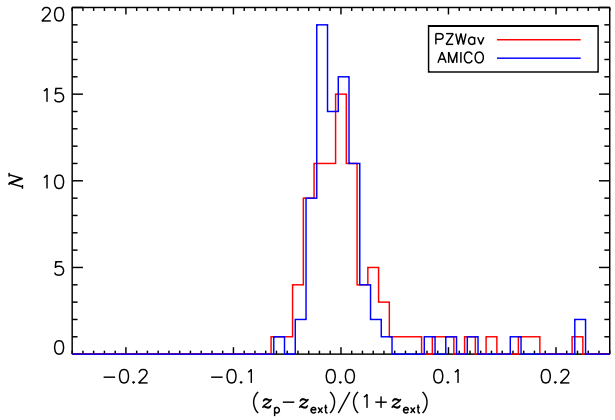

Fig. 11. Histogram of the difference between *Euclid* redshift z_p and external redshift z_{ext} (divided by $1 + z_{ext}$) for `PZWav` and `AMICO` in the EDF-S for the 47 cluster detections matched in various multiwavelength catalogues.

4.3. Centring offsets between Euclid and external data sets

We computed the distances between the positions of the *Euclid* detections and the positions of the matched clusters in the external catalogues. Fig. 12 shows the histograms in the EDF-S for eROSITA (left) and MCSZ (right), for positions taken from `PZWav` (red) and `AMICO` (blue). For eROSITA, a clear peak is visible in the histogram below 200 kpc for `PZWav` and `AMICO`.

For MCSZ, the two histograms show a small peak around 200 kpc. This can be explained by the positional accuracy of the SZ experiments, which has a typical value of a few times 0.′1 for the South Pole Telescope (SPT, see Ruhl et al. 2004) and the Atacama Cosmology Telescope (ACT, see Fowler et al. 2007) clusters, corresponding to about 100 kpc at $z = 0.5$. The positional accuracy of the SZ experiments is lower than the positional accuracy of eROSITA (below 0.′1, and is expected to further smooth the histogram. This effect is related to the fact that

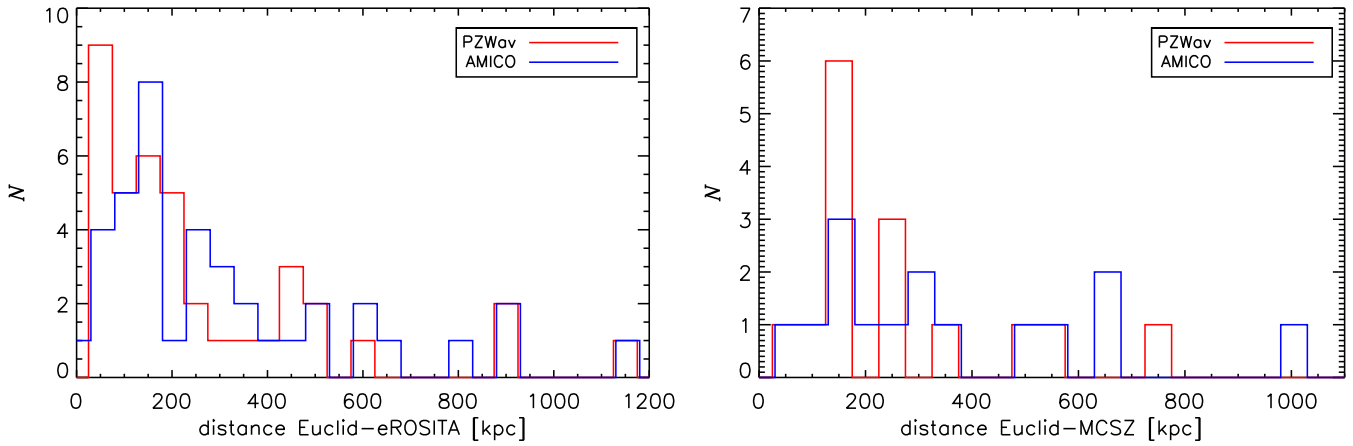

Fig. 12. Centring offsets between *Euclid* catalogues and external catalogues in the EDF-S. The left and right panels refer to eROSITA and MCSZ, respectively.

there are only a small number of matches (15) with MCSZ. We also investigated the dependence of these offsets with the S/N of the detections for each algorithm and found no significant correlation.

4.4. Comparison between Euclid and external cluster observables

For the largest cross-matched population of objects in the EDF-S, in addition to the redshift and positional accuracy, we examined the correlation of the *Euclid* cluster observables – principally the richness – against external mass proxies from multiwavelength data, where available. Fig. 13 highlights the correlation of the *Euclid* richness against three external mass proxies from the DES Y1 `RedMaPPer` and eROSITA data sets, namely the `RedMaPPer` richness, eROSITA-based luminosity, and temperature. For the comparison to eROSITA observables, the richness is computed within the same R_{500} radius. In all cases, a clear correlation is present, with the tightest scatter observed in the direct comparison of richnesses, with a larger, expected scatter for the optical richness compared to the X-ray luminosity, consistent with results shown in Kluge et al. (2024). Finally, the large uncertainties in the X-ray temperatures are due to the limited number of photon counts in the eRASS1 data set.

We also extracted the SZ flux of the 426 *Euclid* detections in the *Planck* legacy maps. We averaged the signal in three bins of *Euclid* richness ($\lambda_{\rm Pmem} < 36.1$, $36.1 < \lambda_{\rm Pmem} < 93.4$, $\lambda_{\rm Pmem} > 93.4$). Results are shown in Fig. 14. The SZ flux in a sphere of R_{500}, Y_{500}, is scaled by $E^{-2/3}(z)[D_{\rm A}(z)/500\,{\rm Mpc}]^2$ to make it proportional to the halo mass M_{500}, where $E(z) = H(z)/H_0$ with $H(z)$ the Hubble parameter. Red diamonds show the result for the full sample.

The SZ signal is detected in the three richness bins. We also present the results for two subsamples: the matched subsample (blue triangles) containing the 110 detections matched with catalogues and meta-catalogues corresponding to numbers in brackets in Table 1; and the unmatched subsample (black squares) containing the remaining 426−110 = 316 detections. The SZ signal is detected with the same amplitude in the highest richness bin (third) for both subsamples. In the lower richness bins (first and second), the signal is detected for the matched subsample but not detected for the unmatched subsample. In particular, the difference in SZ flux between the matched and unmatched detections in the first/second bin is $2.3/3.8\sigma$ respectively, indicating that the unmatched subsample contains significantly less hot gas than the matched subsample for richness $\lambda_{\rm Pmem} < 93.4$. Investigations with deeper SZ observations (e.g. ACT or SPT-3G) and deep X-ray observations (e.g. XMM or eROSITA) will be necessary to quantify better the gas content of the newly discovered *Euclid* detections.

This difference in the gas content of the matched and unmatched subsample with $\lambda_{\rm Pmem} < 93.4$ may be due to the fact that a large fraction of our external catalogues and meta-catalogues are SZ or X-ray selected, so most probably contain gas-rich systems. The unmatched subsample is thus expected to contain more gas-poor systems. It is also possible that projection effects in the *Euclid* detection are boosting richness for intrinsically poor systems, whose mass is consistent with a very low SZ and X-ray signal. While this effect is expected to be marginal for the richest systems (for which SZ flux is comparable for matched and unmatched), it could be significant at lower richness. This result should be compared with the results reported in Popesso et al. (2024), where optically detected (but X-ray undetected) systems identified with eROSITA are predominantly found in filaments, while those detected in X-rays are mainly located in nodes. Recent simulation-based studies supporting this trend are presented in Cui et al. (2024) and Marini et al. (2025).

4.5. Unmatched detections from external data sets

Because the Q1 cluster sample is intended to serve as a first validation of the cluster workflow during the early phase of the *Euclid* mission, it has been constructed on the basis of purity rather than completeness. As a result, we forgo any in-depth analysis on individual clusters from external data sets that are not matched to any of the systems in the Q1 cluster catalogue. Nevertheless, in order to understand the detection limit of the current Q1 sample with respect to external data sets, we construct the histograms of matched and unmatched populations for three external data sets in the EDF-S, because this field contains the largest number of multi-wavelength counterparts; these are the DES Y1 `RedMaPPer`, eROSITA, and MCSZ samples.

Fig. 15 shows the distribution in SZ-based total mass, `RedMaPPer` richness, and eROSITA X-ray based mass estimate, for the matched and unmatched clusters falling within the EDF-S, where the expected coverage is above 80% (see Sect. 2.2). We see a consistent trend across optical, X-ray and millimetre

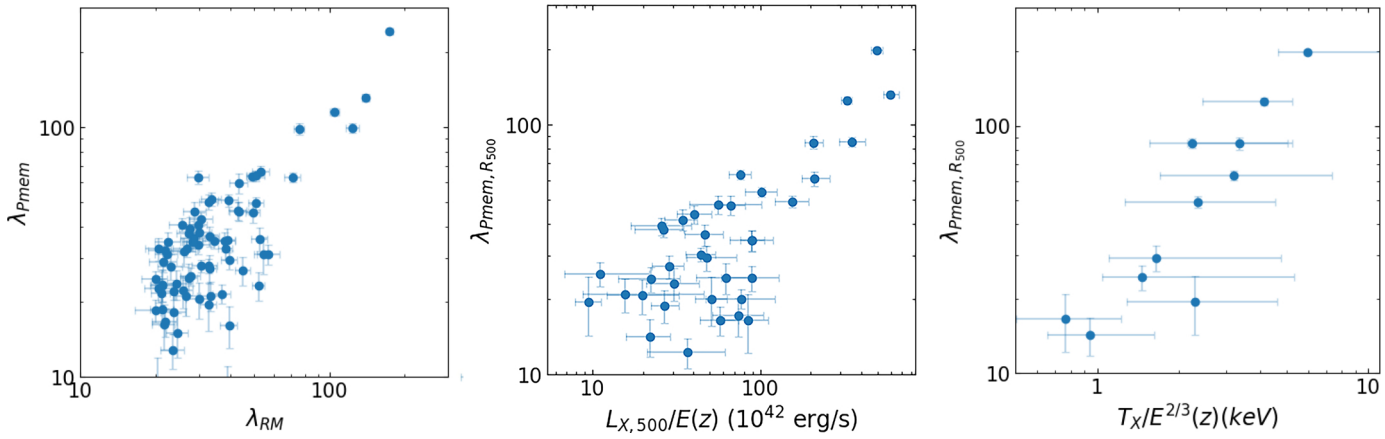

Fig. 13. Correlation of the *Euclid* richness $\lambda_{\rm Pmem}$ against `RedMaPPer` richness (left), eROSITA mass proxies – the X-ray luminosity $L_{X,500}$ (middle) and X-ray temperature $T_{\rm X,500}$ (right) for the matched systems within the EDF-S.

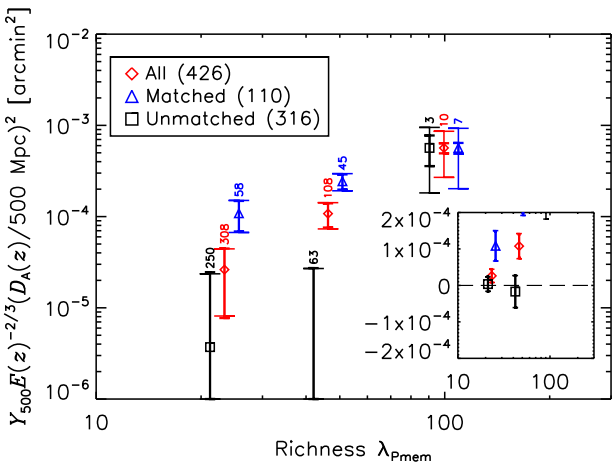

Fig. 14. *Planck* SZ flux versus *Euclid* richness for the full *Euclid* Q1 sample (red diamonds), and for the subsamples matched (blue triangles) and unmatched (black squares) to external catalogues and meta-catalogues. Thick error bars are statistical errors and thin error bars are bootstrap (total) errors. The number on top of each error bar is the number of objects averaged in each bin. The SZ flux is detected by *Planck* in the two highest richness bins for the full sample and in all the three bins for the matched subsample. However, *Planck* does not detect the signal in the unmatched subsample, indicating that it contains significantly less hot gas than the matched subsample.

wavelengths, whereby the unmatched populations systematically occupy the lower richness and lower mass ends of the overall distribution, although within a limited area of approximately 27 square degrees, the statistics are sparse.

Since the joint *Euclid* catalogue is cut at high S/N by construction, it does not completely sample the underlying cluster population, particularly at lower richnesses (78% of the unmatched `RedMaPPer` objects have a richness less than 30). This reinforces the hypothesis that incompleteness in the cluster sample at this stage is largely driven by the high S/N threshold on the individual detection catalogues and the degree of intrinsic scatter shown in Fig. 4, in addition to known issues of incompleteness in the *Euclid* galaxy catalogues at lower redshifts, described in more detail in Klein et al., (in preparation).

4.6. The potential for new Euclid cluster detections

For the consideration of new, potentially undetected clusters in the Q1 fields, we expanded our search beyond the list of catalogues and meta-catalogues described in Sect. 4.1 for the redshift validation and measurement of positional scatter. We performed a cross-match of all the detections within the NASA/IPAC Extragalactic Database (NED)[9], using a matching radius of two arcminutes, and a redshift constraint of $|z_{\rm p} - z_{\rm NED}| < 3\sigma_{z_{\rm p}}$. We also perform a match to the Massive and Distant Clusters of the Wise Survey 2 (MaDCoWS2), described in Thongkham et al. (2024) and Wen and Han 2024 (WH24) cluster catalogue (Wen & Han 2024), using an identical scheme to the one described above, simply replacing the NED redshifts with those from MaDCoWS2/WH24.

After filtering for overlap between the matches retrieved from NED, MaDCoWS2 and/or WH24 with the existing meta catalogues, we find 76, 72, and 91 new matches in the EDF-N, EDF-F, and EDF-S, respectively. Detailed information on the supplementary matches is contained within Appendix B. Subtracting the total number of existing matches in the literature, we report 57, 5, and 15 new detections in the EDF-N, EDF-F, and EDF-S, totaling 77 potentially new *Euclid* clusters. A total of 48 of these systems have a cluster redshift $z_{\rm p} \geq 1$, 36 of which are in EDF-N and 11 in EDF-S.

Each of these new detections was visually inspected in both the *Euclid* imaging data and Dark Energy Spectroscopic Instrument (DESI) Legacy imaging to confirm the presence of a galaxy overdensity and to check for possible contamination of a detection from artefacts or nearby bright stars. We also inspected histograms of the photometric redshifts within 2′ of the cluster centre to look for coherent peaks at the nominal cluster redshift, and used external spectroscopic redshifts to confirm the presence of real clusters. The results of these final checks indicates that 20 out of the total sample of 426 clusters are likely to be spurious.

4.7. Beyond $z \geq 1.5$: the case for Euclid

While we impose an upper redshift limit on our joint cluster sample for this first analysis due to the limitations in photometric redshift estimation described in Sect. 2.3, the detection algorithms as well as the richness estimation are nevertheless applied

[9] NED is funded by the National Aeronautics and Space Administration and operated by the California Institute of Technology.

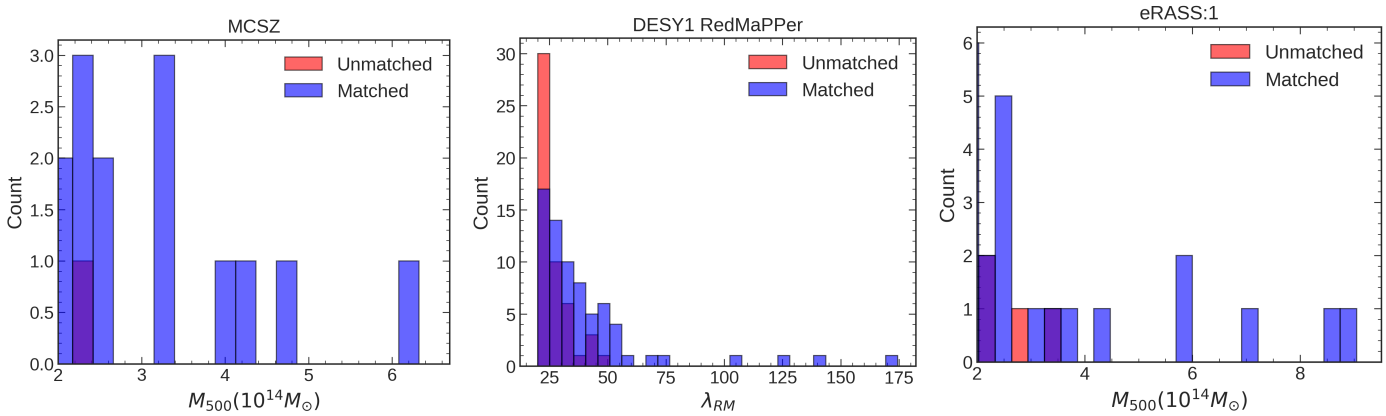

Fig. 15. Histograms of matched and unmatched clusters from external multi-wavelength data sets in the EDF-S – MCSZ (*left*), DES Y1 `RedMaPPer` (*middle*), and eROSITA (*right*). The histograms are shown as a function of SZ-based total mass (M_{500}), optical richness (λ), and X-ray based total mass (M_{500}), respectively.

on the nominal *Euclid* redshift range, which extends to a redshift of $z = 2$. To this end, we study the number of joint clusters which fall in the redshift range $1.5 \leq z \leq 2$ to evaluate their reliability as a means to highlight one of the key scientific goals of *Euclid* – the detection and characterisation of the high redshift cluster population, as Sartoris et al. (2016) showed that formally half of the cosmological constraining power of the *Euclid* cluster survey comes from clusters in the redshift range $1 \leq z \leq 2$. Due to the increased scatter of galaxy photometric redshifts beyond $z \geq 1.5$ and contamination in the galaxy catalogues, we expect strong incompleteness and impurity in this range. However, we present a subsample of promising candidates that were selected based on a combination of S/N above the threshold and visual inspection. Because the purity is low at this epoch for the current catalogue, these represent a small subset of high S/N detections. We anticipate significantly improved purity in this redshift range for DR1.

In total, we find 58 systems across the three fields (four in the EDF-F, 10 in the EDF-S, and 44 in the EDF-N). The asymmetry in the number of detections between the north and south is driven by the apparent higher rate of contamination in the north in this field, in part due to its higher stellar density. We use the same criteria as described in Sect. 4.6 to determine the reliability of these high redshift systems, noting 15 in total, which display clear visual overdensities in *Euclid* and external imaging data where applicable. The complete properties, including positions, redshifts and richness estimates for these 15 systems are shown in Table A.2. We display postage stamps of six examples of these candidates across the three fields in Fig. 16.

5. External spectroscopic validation of clusters

We used the previously mentioned set of publicly available spectroscopic redshifts described in Sect. 2.3 to estimate the spectroscopic redshifts for cluster detections in both the EDF-F and EDF-N. As stated earlier, the spectroscopic coverage of the EDF-S is poor, so we were unable to perform this analysis on that field. Using external spectroscopic data is particularly valuable in the low-redshift regime, which is not covered by *Euclid* spectroscopy.

We selected galaxies with external spectroscopic redshift measurements within a cylinder centred on the cluster coordinates provided by the `AMICO` and `PZWav` detection algorithms. For simplicity, `PZWav` detections are used as the cylinder centres, as similar results would be obtained using `AMICO` detections. The selection radius was initially set to 1 Mpc from the centre, with an initial redshift-space window of $0.1(1+z_{\rm DET})$ centred on $z_{\rm DET}$, where $z_{\rm DET}$ here refers to the photometric redshift measured by `PZWav`.

We focused on the cluster core to identify the peak in redshift space in order to minimise potential line-of-sight contamination in the outskirts. The relatively large initial redshift-space window was chosen to mitigate the bias and scatter previously observed between photometric and spectroscopic redshifts. We also applied a photometric redshift filter to disentangle the spectroscopic counterpart corresponding to the detection peak from potential other concentrations, keeping objects in a photometric redshift window $0.04(1 + z_{\rm DET})$ centred on $z_{\rm DET}$.

The spectroscopic redshift of the cluster was estimated using the biweight technique which has been shown to be appropriate for a small number of objects (Beers et al. 1990). After identifying the peak in redshift space, the criteria in photometric redshift was relaxed, and the radius was increased to 2 Mpc in order to improve statistics. Galaxies with a radial velocity offset larger than $v_r = 3000\,{\rm km\,s^{-1}}$ in the cluster rest frame were rejected. The estimates of the spectroscopic redshift, its error, and the final number of galaxies used within 2 Mpc are provided in Table A.1 for those clusters with more than three redshifts remaining at the end of the procedure (see Fig. 17).

Fig. 18 compares the external spectroscopic redshift estimates with the photometric redshift estimates derived from the detections for the subsample of high-S/N detections in the EDF-F and EDF-N, as previously defined.

Out of 98 (137) cluster candidates with redshift lower than 1.5 in the EDF-F (EDF-N), a spectroscopic redshift was measured for 39(51) of them with more than three members. We found 30 cluster candidates (39) with at least five spectroscopic members (shown in blue), while 9 (12) had three or four members (shown in magenta). Spectroscopic redshift estimates are shown to be in good agreement with the photometric redshift estimates. The relationship between the two estimates is fitted using a parametric model, and the region within one standard deviation is shaded in grey in the Fig. 18. A systematic bias appears in the EDF-F, particularly in the redshift range $z \in [0.5, 0.9]$, and to a lesser extent below redshift $z = 0.7$ in the EDF-N, reflecting the same trend observed in the galaxy sample (Fig. 2).

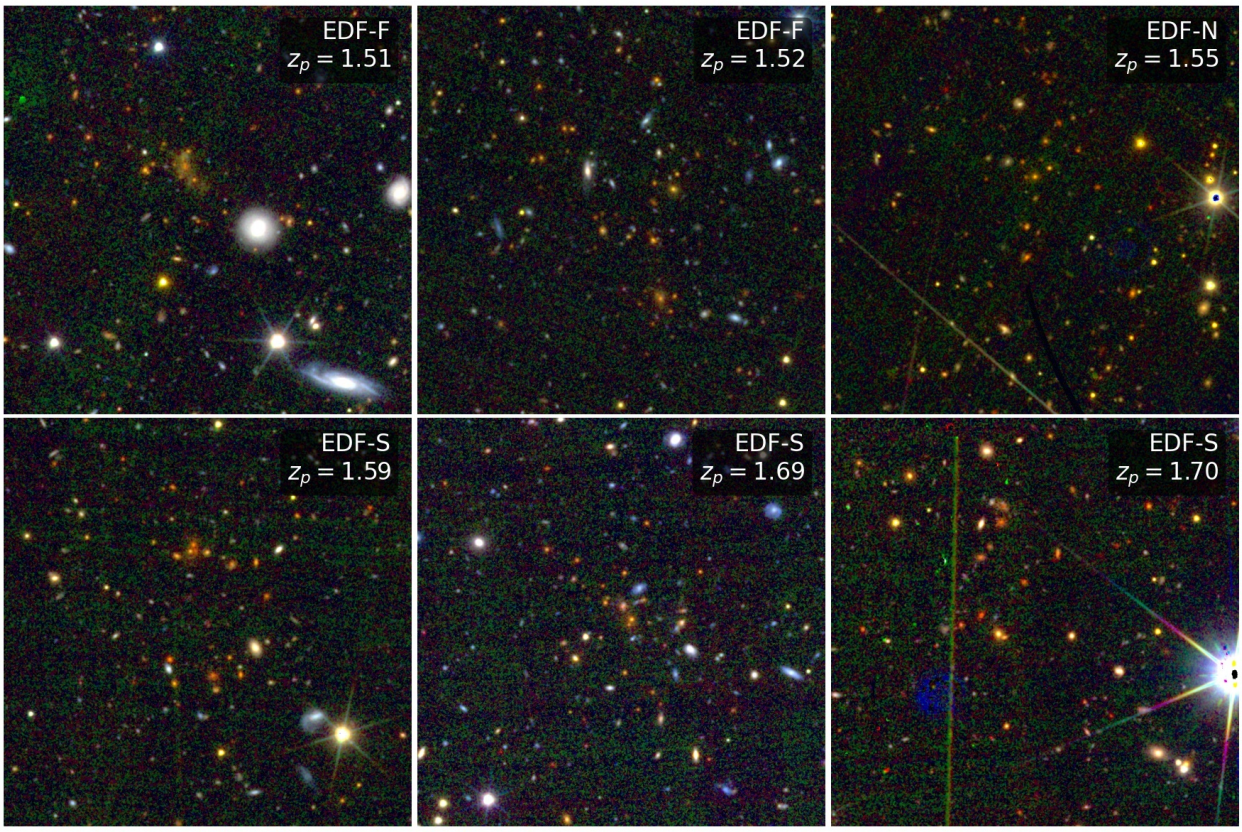

Fig. 16. Postage stamps of $z \geq 1.5$ cluster candidates in the three Q1 fields as described in Sect. 4.7. The properties, including coordinates, redshifts and richnesses for these candidates are displayed in Table A.2.

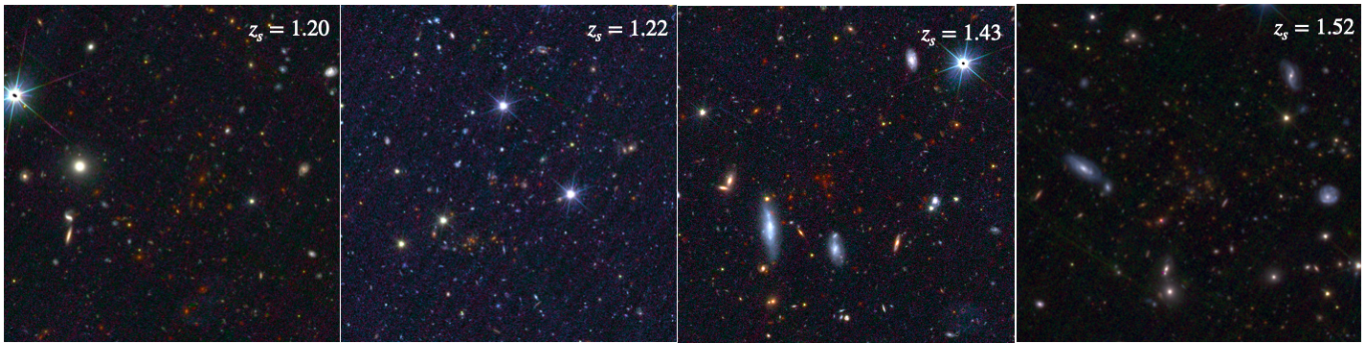

Fig. 17. 2×2 arcminute VIS and NIR band colour cutouts of four *Euclid* cluster detections in the EDF-N with an estimated $z_s \geq 1$ based on at least two reliable spectroscopic redshifts per cluster field, in keeping with the methodology described in Sect. 5. The spectroscopic redshifts shown are derived within an aperture of 2 Mpc from the cluster position. From left to right, the number of galaxies used for the cluster redshift measurement are two, five, four, and two, respectively.

When possible, we performed a supplementary validation of the cluster redshifts using the internal *Euclid* `OU-SPE` framework. However, since the number of concordant galaxies with *Euclid* spectra is below five in all cases, we do not deem this sufficient to spectroscopically confirm the cluster detections. Nevertheless, the values obtained with `OU-SPE` and the *Euclid* photometry are largely consistent; the details of this analysis can be found in Appendix C.

6. Conclusions

We have performed a validation of the *Euclid* cluster workflow on the Q1 data release. We emphasise that this is the first time the workflow has been validated on real *Euclid* data following its extensive testing on the Flagship mock catalogues presented in Cabanac et al. (in prep.). We applied a galaxy selection and extensive validation of photometric quality on the *Euclid* source catalogues for the purposes of optimal cluster detection. Subsequently, we ran the `AMICO` and `PZWav` cluster finders on the three Q1 fields to produce a joint catalogue consisting of 426 high S/N detections identified from the two algorithms in a redshift range $0.2 \leq z_p \leq 1.5$.

We characterise the detections according to their richness, colour-magnitude diagrams, and centring offsets, and we performed visual inspection of each of the sources. We cross-checked the validity of the Q1 catalogue against external

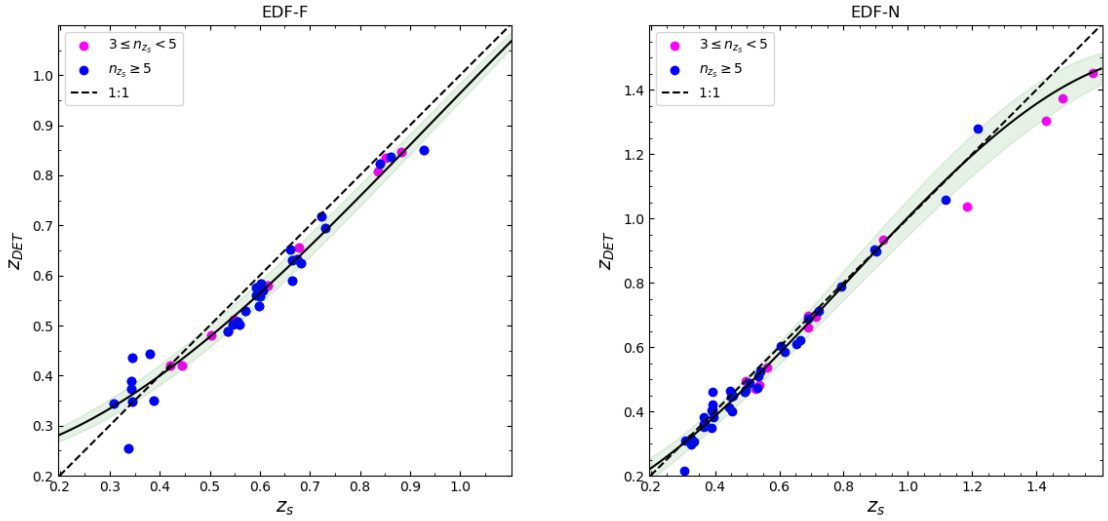

Fig. 18. Spectroscopic redshift versus photometric redshift for high S/N cluster detections covered by spectroscopy in the EDF-F (*left*) and the EDF-N (*right*). Cluster candidates with more than five members are shown in blue, and those with three or four members are shown in magenta. An empirical fit of the $z_{\rm DET}$-z_s relation is shown with a continuous line, along with the 1σ envelope of the residuals (light green).

photometric and spectroscopic data sets, noting that we have favoured purity heavily over completeness for the purposes of a first validation. Nevertheless, we explored the limitations of the *Euclid* detections, driven in part by incompleteness in the galaxy catalogues and large photometric redshift uncertainties at higher redshift.

The detections presented in this paper represent an initial validation of the functionality of the *Euclid* cluster detection workflow, yielding high S/N detections detected by both `AMICO` and `PZWav`. The characterisation of the photometric redshifts, centring, and richnesses further confirms that the detection workflow works as expected.

We have presented an initial catalogue consisting of 426 reliable cluster detections. Of these, 349 clusters have at least one known counterpart, spanning various external catalogues of multi-wavelength data. The remaining 77 are plausible, new candidates without established counterparts in the literature, verified by *Euclid* visual inspection and photometric redshift distributions around the cluster positions. Among them, 8 have a spectroscopic redshift estimated with more than five members within 2 Mpc, so seem to be spectroscopically confirmed.

For all systems reported in this catalogue, we find strong internal agreement between the redshift and centring estimation from the two cluster finders. For the systems matched to external data sets, we find clear, positive correlations of the *Euclid* richness with external mass proxies such as the SZ total mass and X-ray luminosity and temperature.

The main limitations at present arise from residual issues with the input galaxy catalogue that are expected to be resolved by the time of the DR1 release. Specifically, incompleteness in the galaxy catalogue – especially for bright, low-redshift galaxies – and the current large scatter in the photometric redshifts at $z > 1.5$ respectively impact the derived richnesses and limit the catalogue to lower redshifts.

We also foresee improvements in contamination rejection and masking prior to DR1, although both of these concerns are already manageable with the Q1 data set. Because we expect that the external band photometry will improve significantly following the observation of more fields to better calibrate OU-PHZ templates, in addition to bias corrections in the photometric pipeline, we can expect that the results will improve considerably for DR1, whilst already demonstrating a successful application of multiple aspects of the *Euclid* cluster workflow for the detection and characterisation of optically selected galaxy clusters.

Acknowledgements. SB would like to acknowledge support from the Poincaré Fellowship funded by the Observatoire de la Côte d'Azur and the Initiative d'excellence d'Université Côte d'Azur. EM is supported by the PRIN 2022 project 'EMC2 – *Euclid* Mission Cluster Cosmology: unlock the full cosmological utility of the *Euclid* photometric cluster catalog', funded by the European Union – NextGenerationEU, Mission 4, Component 2, Investment 1.1 – CUP C53D23001140006, project code: 2022KCS97B. This work made use of the HEALPix software package (Górski et al. 2005). This work has made use of the *Euclid* Quick Release Q1 data from the *Euclid* mission of the European Space Agency (ESA), 2025, `https://doi.org/10.57780/esa-2853f3b`. The Euclid Consortium acknowledges the European Space Agency and a number of agencies and institutes that have supported the development of *Euclid*, in particular the Agenzia Spaziale Italiana, the Austrian Forschungsförderungsgesellschaft funded through BMK, the Belgian Science Policy, the Canadian Euclid Consortium, the Deutsches Zentrum für Luft- und Raumfahrt, the DTU Space and the Niels Bohr Institute in Denmark, the French Centre National d'Etudes Spatiales, the Fundação para a Ciência e a Tecnologia, the Hungarian Academy of Sciences, the Ministerio de Ciencia, Innovación y Universidades, the National Aeronautics and Space Administration, the National Astronomical Observatory of Japan, the Netherlandse Onderzoekschool Voor Astronomie, the Norwegian Space Agency, the Research Council of Finland, the Romanian Space Agency, the State Secretariat for Education, Research, and Innovation (SERI) at the Swiss Space Office (SSO), and the United Kingdom Space Agency. A complete and detailed list is available on the *Euclid* web site (`www.euclid-ec.org`).

References

Abbott, T. M. C., Aguena, M., Alarcon, A., et al. 2020, Phys. Rev. D, 102, 023509
Abbott, T. M. C., Adamów, M., Aguena, M., et al. 2021, ApJS, 255, 20
Abell, G. O. 1958, ApJS, 3, 211
Abell, G. O., Corwin, H. G., Jr., & Olowin, R. P. 1989, ApJS, 70, 1
Aihara, H., AlSayyad, Y., Ando, M., et al. 2022, PASJ, 74, 247
Andreon, S. 2016, A&A, 587, A158
Beers, T. C., Flynn, K., & Gebhardt, K. 1990, AJ, 100, 32
Bellagamba, F., Roncarelli, M., Maturi, M., & Moscardini, L. 2018, MNRAS, 473, 5221
Bulbul, E., Liu, A., Kluge, M., et al. 2024, A&A, 685, A106
Castignani, G., & Benoist, C. 2016, A&A, 595, A111
Costanzi, M., Saro, A., Bocquet, S., et al. 2021, Phys. Rev. D, 103, 043522
Cui, W., Jennings, F., Dave, R., Babul, A., & Gozaliasl, G. 2024, MNRAS, 534, 1247

Diehl, H. T., Buckley-Geer, E. J., Lindgren, K. A., et al. 2017, ApJS, 232, 15
Euclid Collaboration (Adam, R., et al.) 2019 A&A, 627, A23
Euclid Collaboration (Giocoli, C., et al.) 2024, A&A, 681, A67
Euclid Collaboration (Castander, F. J., et al.) 2025, A&A, 697, A5
Euclid Collaboration (Cropper, M., et al.) 2025, A&A, 697, A2
Euclid Collaboration (Ingoglia, L., et al.) 2025, A&A, 695, A280
Euclid Collaboration (Jahnke, K., et al.) 2025, A&A, 697, A3
Euclid Collaboration (Mellier, Y., et al.) 2025, A&A, 697, A1
Euclid Collaboration (Ragagnin, A., et al.) 2025, A&A, 695, A282
Euclid Collaboration (Aussel, H., et al.) 2026, A&A, 711, A1 (Euclid Q1 SI)
Euclid Collaboration (Bergamini, P., et al.) 2026, A&A, 711, A33 (Euclid Q1 SI)
Euclid Collaboration (Enia, A., et al.) 2026, A&A, 711, A14 (Euclid Q1 SI)
Euclid Collaboration (McCracken, H. J., et al.) 2026, A&A, 711, A2 (Euclid Q1 SI)
Euclid Collaboration (Romelli, E., et al.) 2026, A&A, 711, A4 (Euclid Q1 SI)
Euclid Collaboration (Tucci, M., et al.) 2026, A&A, 711, A5 (Euclid Q1 SI)
Euclid Quick Release Q1 2025, https://doi.org/10.57780/esa-2853f3b
Fioc, M., & Rocca-Volmerange, B. 1997, A&A, 326, 950
Fowler, J. W., Niemack, M. D., Dicker, S. R., et al. 2007, Appl. Opt., 46, 3444
Górski, K. M., Hivon, E., Banday, A. J., et al. 2005, ApJ, 622, 759
Gwyn, S., McConnachie, A. W., Cuillandre, J.-C., et al. 2025, AJ, 170, 324
Kluge, M., Comparat, J., Liu, A., et al. 2024, A&A, 688, A210
Lesci, G. F., Marulli, F., Moscardini, L., et al. 2022, A&A, 659, A88
Lin, Y.-T., Mohr, J. J., Gonzalez, A. H., & Stanford, S. A. 2006, ApJ, 650, L99
Marini, I., Popesso, P., Dolag, K., et al. 2025, A&A, 698, A191
Maturi, M., Bellagamba, F., Radovich, M., et al. 2019, MNRAS, 485, 498
Meneghetti, M., Davoli, G., Bergamini, P., et al. 2020, Science, 369, 1347
Navarro, J. F., Frenk, C. S., & White, S. D. M. 1996, ApJ, 462, 563
Planck Collaboration VI. 2020, A&A, 641, A6
Popesso, P., Biviano, A., Bulbul, E., et al. 2024, MNRAS, 527, 895
Romanello, M., Marulli, F., Moscardini, L., et al. 2025, A&A, 693, A195
Ruhl, J., Ade, P. A. R., Carlstrom, J. E., et al. 2004, in Z-Spec: A Broadband Millimeter-wave Grating Spectrometer: Design, Construction, and First Cryogenic Measurements, eds. C. M. Bradford, P. A. R. Ade, J. E. Aguirre, et al., SPIE Conf. Ser., 5498, 11
Rykoff, E. S., Rozo, E., Hollowood, D., et al. 2016, ApJS, 224, 1
Sadibekova, T., Arnaud, M., Pratt, G. W., Tarrío, P., & Melin, J. B. 2024, A&A, 688, A187
Sartoris, B., Biviano, A., Fedeli, C., et al. 2016, MNRAS, 459, 1764
Schechter, P. 1976, ApJ, 203, 297
Sereno, M. 2015, MNRAS, 450, 3665
Tarrío, P., Melin, J. B., & Arnaud, M. 2019, A&A, 626, A7
Thongkham, K., Gonzalez, A. H., Brodwin, M., et al. 2024, ApJ, 967, 123
Wen, Z. L., & Han, J. L. 2024, ApJS, 272, 39
Werner, S. V., Cypriano, E. S., Gonzalez, A. H., et al. 2023, MNRAS, 519, 2630
Zonca, A., Singer, L., Lenz, D., et al. 2019, J. Open Source Softw., 4, 1298

[1] Université Côte d'Azur, Observatoire de la Côte d'Azur, CNRS, Laboratoire Lagrange, Bd de l'Observatoire, CS 34229, 06304 Nice cedex 4, France
[2] Department of Astronomy, University of Florida, Bryant Space Science Center, Gainesville, FL 32611, USA
[3] Institut für Theoretische Physik, University of Heidelberg, Philosophenweg 16, 69120 Heidelberg, Germany
[4] Zentrum für Astronomie, Universität Heidelberg, Philosophenweg 12, 69120 Heidelberg, Germany
[5] Université Paris-Saclay, CEA, Département de Physique des Particules, 91191, Gif-sur-Yvette, France
[6] Department of Physics and Astronomy, University of California, Davis, CA 95616, USA
[7] INAF-Osservatorio Astronomico di Trieste, Via G. B. Tiepolo 11, 34143 Trieste, Italy
[8] IFPU, Institute for Fundamental Physics of the Universe, Via Beirut 2, 34151 Trieste, Italy
[9] Université Paris Cité, CNRS, Astroparticule et Cosmologie, 75013 Paris, France
[10] Univ. Grenoble Alpes, CNRS, Grenoble INP, LPSC-IN2P3, 53, Avenue des Martyrs, 38000, Grenoble, France
[11] Universität Bonn, Argelander-Institut für Astronomie, Auf dem Hügel 71, 53121 Bonn, Germany
[12] INAF-Osservatorio di Astrofisica e Scienza dello Spazio di Bologna, Via Piero Gobetti 93/3, 40129 Bologna, Italy
[13] INFN-Sezione di Bologna, Viale Berti Pichat 6/2, 40127 Bologna, Italy
[14] Universitäts-Sternwarte München, Fakultät für Physik, Ludwig-Maximilians-Universität München, Scheinerstrasse 1, 81679 München, Germany
[15] INAF-Osservatorio Astronomico di Brera, Via Brera 28, 20122 Milano, Italy
[16] Dipartimento di Fisica – Sezione di Astronomia, Università di Trieste, Via Tiepolo 11, 34131 Trieste, Italy
[17] Institut de Recherche en Astrophysique et Planétologie (IRAP), Université de Toulouse, CNRS, UPS, CNES, 14 Av. Edouard Belin, 31400 Toulouse, France
[18] Max Planck Institute for Extraterrestrial Physics, Giessenbachstr. 1, 85748 Garching, Germany
[19] Université Paris-Saclay, Université Paris Cité, CEA, CNRS, AIM, 91191, Gif-sur-Yvette, France
[20] Department of Physics & Astronomy, University of Sussex, Brighton BN1 9QH, UK
[21] School of Physics and Astronomy, University of Nottingham, University Park, Nottingham NG7 2RD, UK
[22] INAF, Istituto di Radioastronomia, Via Piero Gobetti 101, 40129 Bologna, Italy
[23] Institut d'Astrophysique de Paris, UMR 7095, CNRS, and Sorbonne Université, 98 bis boulevard Arago, 75014 Paris, France
[24] Institut d'Astrophysique de Paris, 98bis Boulevard Arago, 75014, Paris, France
[25] CNRS-UCB International Research Laboratory, Centre Pierre Binetruy, IRL2007, CPB-IN2P3, Berkeley, USA
[26] Dipartimento di Fisica e Astronomia "Augusto Righi" – Alma Mater Studiorum Università di Bologna, Via Piero Gobetti 93/2, 40129 Bologna, Italy
[27] OCA, P.H.C Boulevard de l'Observatoire CS 34229, 06304 Nice Cedex 4, France
[28] Observatorio Astronómico Nacional, IGN, Calle Alfonso XII 3, E-28014 Madrid, Spain
[29] Université Paris-Saclay, CNRS, Institut d'astrophysique spatiale, 91405, Orsay, France
[30] ESAC/ESA, Camino Bajo del Castillo, s/n., Urb. Villafranca del Castillo, 28692 Villanueva de la Cañada, Madrid, Spain
[31] School of Mathematics and Physics, University of Surrey, Guildford, Surrey, GU2 7XH, UK
[32] INFN, Sezione di Trieste, Via Valerio 2, 34127 Trieste TS, Italy
[33] SISSA, International School for Advanced Studies, Via Bonomea 265, 34136 Trieste TS, Italy
[34] Dipartimento di Fisica e Astronomia, Università di Bologna, Via Gobetti 93/2, 40129 Bologna, Italy
[35] INAF-Osservatorio Astronomico di Padova, Via dell'Osservatorio 5, 35122 Padova, Italy
[36] Space Science Data Center, Italian Space Agency, Via del Politecnico snc, 00133 Roma, Italy
[37] Dipartimento di Fisica, Università di Genova, Via Dodecaneso 33, 16146, Genova, Italy
[38] INFN-Sezione di Genova, Via Dodecaneso 33, 16146, Genova, Italy
[39] Department of Physics "E. Pancini", University Federico II, Via Cinthia 6, 80126, Napoli, Italy
[40] INAF-Osservatorio Astronomico di Capodimonte, Via Moiariello 16, 80131 Napoli, Italy
[41] Instituto de Astrofísica e Ciências do Espaço, Universidade do Porto, CAUP, Rua das Estrelas, PT4150-762 Porto, Portugal
[42] Faculdade de Ciências da Universidade do Porto, Rua do Campo de Alegre, 4150-007 Porto, Portugal
[43] Dipartimento di Fisica, Università degli Studi di Torino, Via P. Giuria 1, 10125 Torino, Italy
[44] INFN-Sezione di Torino, Via P. Giuria 1, 10125 Torino, Italy
[45] INAF-Osservatorio Astrofisico di Torino, Via Osservatorio 20, 10025 Pino Torinese (TO), Italy
[46] INAF-IASF Milano, Via Alfonso Corti 12, 20133 Milano, Italy
[47] Centro de Investigaciones Energéticas, Medioambientales y Tecnológicas (CIEMAT), Avenida Complutense 40, 28040 Madrid, Spain
[48] Port d'Informació Científica, Campus UAB, C. Albareda s/n, 08193 Bellaterra (Barcelona), Spain

[49] Institute for Theoretical Particle Physics and Cosmology (TTK), RWTH Aachen University, 52056 Aachen, Germany
[50] INAF-Osservatorio Astronomico di Roma, Via Frascati 33, 00078 Monteporzio Catone, Italy
[51] INFN section of Naples, Via Cinthia 6, 80126, Napoli, Italy
[52] Institute for Astronomy, University of Hawaii, 2680 Woodlawn Drive, Honolulu, HI 96822, USA
[53] Dipartimento di Fisica e Astronomia "Augusto Righi" – Alma Mater Studiorum Università di Bologna, Viale Berti Pichat 6/2, 40127 Bologna, Italy
[54] Instituto de Astrofísica de Canarias, Vía Láctea, 38205 La Laguna, Tenerife, Spain
[55] Institute for Astronomy, University of Edinburgh, Royal Observatory, Blackford Hill, Edinburgh EH9 3HJ, UK
[56] Jodrell Bank Centre for Astrophysics, Department of Physics and Astronomy, University of Manchester, Oxford Road, Manchester M13 9PL, UK
[57] European Space Agency/ESRIN, Largo Galileo Galilei 1, 00044 Frascati, Roma, Italy
[58] Université Claude Bernard Lyon 1, CNRS/IN2P3, IP2I Lyon, UMR 5822, Villeurbanne, F-69100, France
[59] Institut de Ciències del Cosmos (ICCUB), Universitat de Barcelona (IEEC-UB), Martí i Franquès 1, 08028 Barcelona, Spain
[60] Institució Catalana de Recerca i Estudis Avançats (ICREA), Passeig de Lluís Companys 23, 08010 Barcelona, Spain
[61] UCB Lyon 1, CNRS/IN2P3, IUF, IP2I Lyon, 4 rue Enrico Fermi, 69622 Villeurbanne, France
[62] Mullard Space Science Laboratory, University College London, Holmbury St Mary, Dorking, Surrey RH5 6NT, UK
[63] Departamento de Física, Faculdade de Ciências, Universidade de Lisboa, Edifício C8, Campo Grande, PT1749-016 Lisboa, Portugal
[64] Instituto de Astrofísica e Ciências do Espaço, Faculdade de Ciências, Universidade de Lisboa, Campo Grande, 1749-016 Lisboa, Portugal
[65] Department of Astronomy, University of Geneva, ch. d'Ecogia 16, 1290 Versoix, Switzerland
[66] INAF-Istituto di Astrofisica e Planetologia Spaziali, Via del Fosso del Cavaliere, 100, 00100 Roma, Italy
[67] INFN-Padova, Via Marzolo 8, 35131 Padova, Italy
[68] Aix-Marseille Université, CNRS/IN2P3, CPPM, Marseille, France
[69] INFN-Bologna, Via Irnerio 46, 40126 Bologna, Italy
[70] Institut d'Estudis Espacials de Catalunya (IEEC), Edifici RDIT, Campus UPC, 08860 Castelldefels, Barcelona, Spain
[71] Institute of Space Sciences (ICE, CSIC), Campus UAB, Carrer de Can Magrans, s/n, 08193 Barcelona, Spain
[72] School of Physics, HH Wills Physics Laboratory, University of Bristol, Tyndall Avenue, Bristol, BS8 1TL, UK
[73] FRACTAL S.L.N.E., calle Tulipán 2, Portal 13 1A, 28231, Las Rozas de Madrid, Spain
[74] Dipartimento di Fisica "Aldo Pontremoli", Università degli Studi di Milano, Via Celoria 16, 20133 Milano, Italy
[75] INFN-Sezione di Milano, Via Celoria 16, 20133 Milano, Italy
[76] NRC Herzberg, 5071 West Saanich Rd, Victoria, BC V9E 2E7, Canada
[77] Institute of Theoretical Astrophysics, University of Oslo, P.O. Box 1029 Blindern, 0315 Oslo, Norway
[78] Leiden Observatory, Leiden University, Einsteinweg 55, 2333 CC Leiden, The Netherlands
[79] Jet Propulsion Laboratory, California Institute of Technology, 4800 Oak Grove Drive, Pasadena, CA, 91109, USA
[80] Felix Hormuth Engineering, Goethestr. 17, 69181 Leimen, Germany
[81] Technical University of Denmark, Elektrovej 327, 2800 Kgs. Lyngby, Denmark
[82] Cosmic Dawn Center (DAWN), Denmark
[83] Université Paris-Saclay, CNRS/IN2P3, IJCLab, 91405 Orsay, France
[84] Max-Planck-Institut für Astronomie, Königstuhl 17, 69117 Heidelberg, Germany
[85] NASA Goddard Space Flight Center, Greenbelt, MD 20771, USA
[86] Department of Physics and Astronomy, University College London, Gower Street, London WC1E 6BT, UK
[87] Department of Physics and Helsinki Institute of Physics, Gustaf Hällströmin katu 2, 00014 University of Helsinki, Finland
[88] Université de Genève, Département de Physique Théorique and Centre for Astroparticle Physics, 24 quai Ernest-Ansermet, CH-1211 Genève 4, Switzerland
[89] Department of Physics, P.O. Box 64, 00014 University of Helsinki, Finland
[90] Helsinki Institute of Physics, Gustaf Hällströmin katu 2, University of Helsinki, Helsinki, Finland
[91] Centre de Calcul de l'IN2P3/CNRS, 21 avenue Pierre de Coubertin 69627 Villeurbanne Cedex, France
[92] Laboratoire d'étude de l'Univers et des phénoménes eXtrêmes, Observatoire de Paris, Université PSL, Sorbonne Université, CNRS, 92190 Meudon, France
[93] Aix-Marseille Université, CNRS, CNES, LAM, Marseille, France
[94] SKA Observatory, Jodrell Bank, Lower Withington, Macclesfield, Cheshire SK11 9FT, UK
[95] University of Applied Sciences and Arts of Northwestern Switzerland, School of Computer Science, 5210 Windisch, Switzerland
[96] INFN-Sezione di Roma, Piazzale Aldo Moro, 2 – c/o Dipartimento di Fisica, Edificio G. Marconi, 00185 Roma, Italy
[97] Department of Physics, Institute for Computational Cosmology, Durham University, South Road, Durham, DH1 3LE, UK
[98] University of Applied Sciences and Arts of Northwestern Switzerland, School of Engineering, 5210 Windisch, Switzerland
[99] Institute of Physics, Laboratory of Astrophysics, Ecole Polytechnique Fédérale de Lausanne (EPFL), Observatoire de Sauverny, 1290 Versoix, Switzerland
[100] Aurora Technology for European Space Agency (ESA), Camino bajo del Castillo, s/n, Urbanizacion Villafranca del Castillo, Villanueva de la Cañada, 28692 Madrid, Spain
[101] Institut de Física d'Altes Energies (IFAE), The Barcelona Institute of Science and Technology, Campus UAB, 08193 Bellaterra (Barcelona), Spain
[102] European Space Agency/ESTEC, Keplerlaan 1, 2201 AZ Noordwijk, The Netherlands
[103] School of Mathematics, Statistics and Physics, Newcastle University, Herschel Building, Newcastle-upon-Tyne, NE1 7RU, UK
[104] DARK, Niels Bohr Institute, University of Copenhagen, Jagtvej 155, 2200 Copenhagen, Denmark
[105] Waterloo Centre for Astrophysics, University of Waterloo, Waterloo, Ontario N2L 3G1, Canada
[106] Department of Physics and Astronomy, University of Waterloo, Waterloo, Ontario N2L 3G1, Canada
[107] Perimeter Institute for Theoretical Physics, Waterloo, Ontario N2L 2Y5, Canada
[108] Centre National d'Etudes Spatiales – Centre spatial de Toulouse, 18 avenue Edouard Belin, 31401 Toulouse Cedex 9, France
[109] Institute of Space Science, Str. Atomistilor, nr. 409 Măgurele, Ilfov, 077125, Romania
[110] Consejo Superior de Investigaciones Cientificas, Calle Serrano 117, 28006 Madrid, Spain
[111] Universidad de La Laguna, Departamento de Astrofísica, 38206 La Laguna, Tenerife, Spain
[112] Dipartimento di Fisica e Astronomia "G. Galilei", Università di Padova, Via Marzolo 8, 35131 Padova, Italy
[113] Université St Joseph; Faculty of Sciences, Beirut, Lebanon
[114] Departamento de Física, FCFM, Universidad de Chile, Blanco Encalada 2008, Santiago, Chile
[115] Universität Innsbruck, Institut für Astro- und Teilchenphysik, Technikerstr. 25/8, 6020 Innsbruck, Austria
[116] Satlantis, University Science Park, Sede Bld 48940, Leioa-Bilbao, Spain
[117] Centre for Electronic Imaging, Open University, Walton Hall, Milton Keynes, MK7 6AA, UK
[118] Instituto de Astrofísica e Ciências do Espaço, Faculdade de Ciências, Universidade de Lisboa, Tapada da Ajuda, 1349-018 Lisboa, Portugal

[119] Cosmic Dawn Center (DAWN)
[120] Niels Bohr Institute, University of Copenhagen, Jagtvej 128, 2200 Copenhagen, Denmark
[121] Universidad Politécnica de Cartagena, Departamento de Electrónica y Tecnología de Computadoras, Plaza del Hospital 1, 30202 Cartagena, Spain
[122] Kapteyn Astronomical Institute, University of Groningen, PO Box 800, 9700 AV Groningen, The Netherlands
[123] Infrared Processing and Analysis Center, California Institute of Technology, Pasadena, CA 91125, USA
[124] Dipartimento di Fisica e Scienze della Terra, Università degli Studi di Ferrara, Via Giuseppe Saragat 1, 44122 Ferrara, Italy
[125] Istituto Nazionale di Fisica Nucleare, Sezione di Ferrara, Via Giuseppe Saragat 1, 44122 Ferrara, Italy
[126] School of Physics and Astronomy, Cardiff University, The Parade, Cardiff, CF24 3AA, UK
[127] Department of Physics, Oxford University, Keble Road, Oxford OX1 3RH, UK
[128] INAF – Osservatorio Astronomico di Brera, Via Emilio Bianchi 46, 23807 Merate, Italy
[129] INAF-Osservatorio Astronomico di Brera, Via Brera 28, 20122 Milano, Italy, and INFN-Sezione di Genova, Via Dodecaneso 33, 16146, Genova, Italy
[130] ICL, Junia, Université Catholique de Lille, LITL, 59000 Lille, France
[131] ICSC – Centro Nazionale di Ricerca in High Performance Computing, Big Data e Quantum Computing, Via Magnanelli 2, Bologna, Italy
[132] Instituto de Física Teórica UAM-CSIC, Campus de Cantoblanco, 28049 Madrid, Spain
[133] CERCA/ISO, Department of Physics, Case Western Reserve University, 10900 Euclid Avenue, Cleveland, OH 44106, USA
[134] Technical University of Munich, TUM School of Natural Sciences, Physics Department, James-Franck-Str. 1, 85748 Garching, Germany
[135] Max-Planck-Institut für Astrophysik, Karl-Schwarzschild-Str. 1, 85748 Garching, Germany
[136] Laboratoire Univers et Théorie, Observatoire de Paris, Université PSL, Université Paris Cité, CNRS, 92190 Meudon, France
[137] Departamento de Física Fundamental. Universidad de Salamanca. Plaza de la Merced s/n. 37008 Salamanca, Spain
[138] Université de Strasbourg, CNRS, Observatoire astronomique de Strasbourg, UMR 7550, 67000 Strasbourg, France
[139] Center for Data-Driven Discovery, Kavli IPMU (WPI), UTIAS, The University of Tokyo, Kashiwa, Chiba 277-8583, Japan
[140] Ludwig-Maximilians-University, Schellingstrasse 4, 80799 Munich, Germany
[141] Max-Planck-Institut für Physik, Boltzmannstr. 8, 85748 Garching, Germany
[142] California Institute of Technology, 1200 E California Blvd, Pasadena, CA 91125, USA
[143] Department of Physics & Astronomy, University of California Irvine, Irvine CA 92697, USA
[144] Department of Mathematics and Physics E. De Giorgi, University of Salento, Via per Arnesano, CP-I93, 73100, Lecce, Italy
[145] INFN, Sezione di Lecce, Via per Arnesano, CP-193, 73100, Lecce, Italy
[146] INAF-Sezione di Lecce, c/o Dipartimento Matematica e Fisica, Via per Arnesano, 73100, Lecce, Italy
[147] Departamento Física Aplicada, Universidad Politécnica de Cartagena, Campus Muralla del Mar, 30202 Cartagena, Murcia, Spain
[148] Instituto de Astrofísica de Canarias (IAC); Departamento de Astrofísica, Universidad de La Laguna (ULL), 38200, La Laguna, Tenerife, Spain
[149] Instituto de Física de Cantabria, Edificio Juan Jordá, Avenida de los Castros, 39005 Santander, Spain
[150] Observatorio Nacional, Rua General Jose Cristino, 77-Bairro Imperial de Sao Cristovao, Rio de Janeiro, 20921-400, Brazil
[151] Institute of Cosmology and Gravitation, University of Portsmouth, Portsmouth PO1 3FX, UK
[152] Department of Computer Science, Aalto University, PO Box 15400, Espoo, FI-00 076, Finland
[153] Instituto de Astrofísica de Canarias, c/ Via Lactea s/n, La Laguna 38200, Spain. Departamento de Astrofísica de la Universidad de La Laguna, Avda. Francisco Sanchez, La Laguna, 38200, Spain
[154] Ruhr University Bochum, Faculty of Physics and Astronomy, Astronomical Institute (AIRUB), German Centre for Cosmological Lensing (GCCL), 44780 Bochum, Germany
[155] Department of Physics and Astronomy, Vesilinnantie 5, 20014 University of Turku, Finland
[156] Serco for European Space Agency (ESA), Camino bajo del Castillo, s/n, Urbanizacion Villafranca del Castillo, Villanueva de la Cañada, 28692 Madrid, Spain
[157] ARC Centre of Excellence for Dark Matter Particle Physics, Melbourne, Australia
[158] Centre for Astrophysics & Supercomputing, Swinburne University of Technology, Hawthorn, Victoria 3122, Australia
[159] Department of Physics and Astronomy, University of the Western Cape, Bellville, Cape Town, 7535, South Africa
[160] DAMTP, Centre for Mathematical Sciences, Wilberforce Road, Cambridge CB3 0WA, UK
[161] Kavli Institute for Cosmology Cambridge, Madingley Road, Cambridge, CB3 0HA, UK
[162] Department of Astrophysics, University of Zurich, Winterthurerstrasse 190, 8057 Zurich, Switzerland
[163] Department of Physics, Centre for Extragalactic Astronomy, Durham University, South Road, Durham, DH1 3LE, UK
[164] IRFU, CEA, Université Paris-Saclay 91191 Gif-sur-Yvette Cedex, France
[165] Oskar Klein Centre for Cosmoparticle Physics, Department of Physics, Stockholm University, Stockholm, SE-106 91, Sweden
[166] Astrophysics Group, Blackett Laboratory, Imperial College London, London SW7 2AZ, UK
[167] INAF-Osservatorio Astrofisico di Arcetri, Largo E. Fermi 5, 50125, Firenze, Italy
[168] Dipartimento di Fisica, Sapienza Università di Roma, Piazzale Aldo Moro 2, 00185 Roma, Italy
[169] Centro de Astrofísica da Universidade do Porto, Rua das Estrelas, 4150-762 Porto, Portugal
[170] Dipartimento di Fisica, Università di Roma Tor Vergata, Via della Ricerca Scientifica 1, Roma, Italy
[171] INFN, Sezione di Roma 2, Via della Ricerca Scientifica 1, Roma, Italy
[172] HE Space for European Space Agency (ESA), Camino bajo del Castillo, s/n, Urbanizacion Villafranca del Castillo, Villanueva de la Cañada, 28692 Madrid, Spain
[173] Department of Astrophysical Sciences, Peyton Hall, Princeton University, Princeton, NJ 08544, USA
[174] Theoretical astrophysics, Department of Physics and Astronomy, Uppsala University, Box 515, 751 20 Uppsala, Sweden
[175] Mathematical Institute, University of Leiden, Einsteinweg 55, 2333 CA Leiden, The Netherlands
[176] Institute of Astronomy, University of Cambridge, Madingley Road, Cambridge CB3 0HA, UK
[177] Space physics and astronomy research unit, University of Oulu, Pentti Kaiteran katu 1, FI-90014 Oulu, Finland
[178] Center for Computational Astrophysics, Flatiron Institute, 162 5th Avenue, 10010, New York, NY, USA
[179] Department of Physics and Astronomy, University of British Columbia, Vancouver, BC V6T 1Z1, Canada

Appendix A: The joint *Euclid* cluster catalogue

Table A.1. The joint *Euclid* cluster catalogue. Subset of 35 PZWav and AMICO-detected clusters with the highest signal-to-noise ratios.

NAME	ID	RA_{PZWav} (degrees)	Dec_{PZWav} (degrees)	RA_{AMICO} (degrees)	Dec_{AMICO} (degrees)	z_{PZWav}	z_{AMICO}	z_{spec}	N_{zspec} (< 2 Mpc)	SNR_{PZWav}	SNR_{AMICO}	λ_{Pmem}
EUCL-Q1-CL J041113.88−481928.2	EUCL-Q1-CL-0	62.8089	−48.3245	62.8067	−48.3245	0.41	0.40	-	-	40.81	89.38	241.47±4.79
EUCL-Q1-CL J041724.90−474849.7	EUCL-Q1-CL-1	64.3521	−47.8150	64.3554	−47.8127	0.55	0.56	-	-	24.20	60.43	115.26±4.13
EUCL-Q1-CL J033747.63−275112.8	EUCL-Q1-CL-2	54.4491	−27.8497	54.4478	−27.8574	0.49	0.48	0.535±0.004	10	23.43	51.72	81.36±4.74
EUCL-Q1-CL J032321.22−275105.3	EUCL-Q1-CL-3	50.8371	−27.8549	50.8397	−27.8481	0.42	0.41	-	-	22.61	46.43	56.14±4.73
EUCL-Q1-CL J040151.05−502848.7	EUCL-Q1-CL-4	60.4686	−50.4780	60.4568	−50.4824	0.43	0.42	-	-	22.38	30.49	99.03±4.45
EUCL-Q1-CL J040558.72−491549.3	EUCL-Q1-CL-5	61.5018	−49.2626	61.4875	−49.2648	0.31	0.30	-	-	22.21	52.78	131.57±4.40
EUCL-Q1-CL J040655.77−480504.2	EUCL-Q1-CL-6	61.7282	−48.0850	61.7365	−48.0840	0.69	0.70	-	-	22.14	34.27	99.21±3.72
EUCL-Q1-CL J041343.51−480756.5	EUCL-Q1-CL-7	63.4322	−48.1305	63.4304	−48.1343	1.47	1.46	-	-	21.74	37.54	22.95±2.24
EUCL-Q1-CL J180607.67+635615.6	EUCL-Q1-CL-8	271.5285	63.9386	271.5355	63.9367	1.32	1.33	-	-	21.53	57.26	23.13±2.05
EUCL-Q1-CL J040509.84−464902.4	EUCL-Q1-CL-9	61.2955	−46.8097	61.2865	−46.8250	0.42	0.38	-	-	20.48	37.06	99.49±4.55
EUCL-Q1-CL J035146.84−480404.3	EUCL-Q1-CL-10	57.9409	−48.0683	57.9494	−48.0674	0.56	0.56	-	-	20.22	35.70	28.75±2.73
EUCL-Q1-CL J034959.80−481952.6	EUCL-Q1-CL-11	57.5029	−48.3288	57.4954	−48.3338	1.40	1.44	-	-	20.14	31.49	60.20±1.75
EUCL-Q1-CL J035003.59−504145.7	EUCL-Q1-CL-12	57.5123	−50.6948	57.5176	−50.6973	0.65	0.66	-	-	20.10	23.28	33.66±2.74
EUCL-Q1-CL J033352.73−272113.8	EUCL-Q1-CL-13	53.4665	−27.3535	53.4728	−27.3542	0.57	0.55	0.605±0.005	8	19.98	36.64	45.67±3.15
EUCL-Q1-CL J032929.78−281930.3	EUCL-Q1-CL-14	52.3730	−28.3266	52.3752	−28.3236	0.63	0.66	0.682±0.007	37	19.74	29.01	59.93±4.68
EUCL-Q1-CL J033412.98−282418.7	EUCL-Q1-CL-15	53.5511	−28.4065	53.5570	−28.4039	0.65	0.66	0.662±0.007	74	18.84	25.32	97.08±2.75
EUCL-Q1-CL J033355.96−283807.7	EUCL-Q1-CL-16	53.4879	−28.6368	53.4785	−28.6342	0.59	0.56	0.665±0.007	38	18.70	25.15	71.24±3.38
EUCL-Q1-CL J040440.54−472444.6	EUCL-Q1-CL-17	61.1691	−47.4098	61.1687	−47.4150	0.88	0.89	-	-	18.62	33.87	50.03±3.70
EUCL-Q1-CL J033619.94−263512.9	EUCL-Q1-CL-18	54.0817	−26.5831	54.0844	−26.5907	0.50	0.50	0.546±0.006	11	17.66	27.53	42.73±2.41
EUCL-Q1-CL J033635.31−292553.3	EUCL-Q1-CL-19	54.1464	−29.4327	54.1478	−29.4303	0.87	0.90	-	-	17.47	30.25	42.64±3.09
EUCL-Q1-CL J041838.86−455252.9	EUCL-Q1-CL-20	64.6645	−45.8807	64.6593	−45.8821	0.69	0.62	-	-	17.19	30.79	76.28±4.23
EUCL-Q1-CL J033851.49−284807.8	EUCL-Q1-CL-21	54.7174	−28.7999	54.7117	−28.8045	1.04	1.04	-	-	16.97	24.47	44.61±2.97
EUCL-Q1-CL J042117.89−484550.8	EUCL-Q1-CL-22	65.3239	−48.7647	65.3252	−48.7635	1.33	1.39	-	-	16.82	23.87	33.74±1.83
EUCL-Q1-CL J033526.63−291824.9	EUCL-Q1-CL-23	53.8620	−29.3015	53.8599	−29.3124	0.51	0.51	0.555±0.010	9	16.51	34.45	39.71±3.00
EUCL-Q1-CL J175712.26+680259.0	EUCL-Q1-CL-24	269.3108	68.0460	269.2914	68.0535	0.38	0.40	-	-	16.46	31.82	43.42±4.31
EUCL-Q1-CL J033538.84−270305.5	EUCL-Q1-CL-25	53.9143	−27.0511	53.9094	−27.0520	0.35	0.35	0.344±0.002	11	16.43	34.13	50.39±4.01
EUCL-Q1-CL J041109.36−490953.7	EUCL-Q1-CL-26	62.7910	−49.1650	62.7870	−49.1649	0.42	0.35	-	-	16.42	31.19	31.01±5.12
EUCL-Q1-CL J034251.87−491114.0	EUCL-Q1-CL-27	55.7173	−49.1902	55.7150	−49.1842	1.40	1.49	-	-	16.38	31.36	30.49±1.25
EUCL-Q1-CL J040406.81−481302.2	EUCL-Q1-CL-28	61.0243	−48.2198	61.0324	−48.2148	0.44	0.40	-	-	16.37	38.93	98.53±5.27
EUCL-Q1-CL J033055.76−294746.3	EUCL-Q1-CL-29	52.7296	−29.7977	52.7351	−29.7948	0.84	0.84	-	-	16.36	21.79	38.51±2.72
EUCL-Q1-CL J034001.03−284959.7	EUCL-Q1-CL-30	55.0111	−28.8358	54.9975	−28.8307	0.25	0.32	0.337±0.004	34	16.23	23.99	17.76±2.84
EUCL-Q1-CL J041839.71−483832.0	EUCL-Q1-CL-31	64.6662	−48.6298	64.6647	−48.6547	1.41	1.50	-	-	16.19	18.74	34.17±2.46
EUCL-Q1-CL J174731.98+663438.5	EUCL-Q1-CL-32	266.8740	66.5803	266.8924	66.5744	0.42	0.42	0.392±0.007	7	15.96	55.86	14.38±2.76
EUCL-Q1-CL J181458.48+645725.1	EUCL-Q1-CL-33	273.7412	64.9563	273.7461	64.9577	0.52	0.52	-	-	15.86	28.17	36.98±3.22
EUCL-Q1-CL J040332.81−482819.1	EUCL-Q1-CL-34	60.8779	−48.4695	60.8955	−48.4745	0.37	0.36	-	-	15.85	36.24	63.50±2.45

Notes. z_{spec} is the estimate of the spectroscopic cluster redshift from external spectroscopy data derived with the methodology detailed in Sect. 5.

Appendix B: Detailed breakdown of Q1 cluster matches to external data sets

In order to perform the external validation of the Q1 cluster sample, the Q1 clusters were matched to various existing data sets using the methodology outlined in Sect. 4. The tables detailed in this Appendix illustrate the breakdown of matches from the meta-catalogues in this analysis, and contains the results from the extended search detailed in Sect. 4.6, from which the assessment of potentially new *Euclid* clusters has been determined.

Appendix C: Spectroscopic validation with OU-SPE

The detection algorithms estimate cluster redshifts based on the mean photometric redshift of member galaxies. To confirm and further refine these estimates, we examined the *Euclid* spectroscopy of galaxies in the cluster fields, as provided in the Q1 data release. We limited our inspections of the *Euclid* spectroscopy to those candidate clusters with $z_{\rm DET} > 0.9$, the lower limit at which the Hα lines can be detected given the spectral sensitivity range of the *Euclid* red grism (Euclid Collaboration: Mellier et al. 2025). This leaves us with 100 cluster candidates (17 in the EDF-F, 43 in the EDF-S, and 40 in the EDF-N).

The *Euclid* OU-SPE package provides five z estimates for each galaxy; in the following, we only use the highest ranked estimate – `spec.spec_rank=0` in the SAS – when selecting objects for verification of their spectroscopic redshifts. We restrict our analysis to galaxies with OU-SPE redshift estimates with signal-to-noise ratio (`spe_line_snr_gf` in the SAS) > 3.5, probability (`spe_z_prob` in the SAS), > 0.99, with line flux $< 10^{-14}$ erg cm^{-2} s^{-1} to avoid spurious features, and based on more than 300 pixels (`spe_npix>300`). Of the galaxies passing these spectroscopic quality criteria, we only considered those within 4 arcmin from the candidate cluster centre (corresponding to $\simeq 2$ Mpc in the range $z = 0.9 - 1.5$), and with spectroscopic redshifts within a range of $\pm 0.05 \times (1 + z_{\rm DET})$, corresponding to about three times the estimated pre-launch cluster $z_{\rm DET}$ uncertainty (Euclid Collaboration: Adam et al. 2019).

In total, we selected 527 galaxies (87 in EDF-F, 197 in EDF-S, and 243 in EDF-N), and after visual inspection of their spectra we retained 170 redshift estimates as reliable (35 in EDF-F, 65 in EDF-S, and 70 in EDF-N), that is, one third of the total. This means we deal with, on average, less than two reliable redshifts per cluster field.

We then look for concordant redshifts in each cluster field, where by 'concordant' we mean that their redshifts must be separated by $\leq 0.0133\,(1 + z_{\rm DET})$, which corresponds to a velocity separation of 4000 km s^{-1} in the cluster rest frame. This value corresponds to $\sim \pm 3$ times the velocity dispersion of a Virgo-like cluster. We were able to identify ≥ 2 concordant-z members in 20 cluster candidates, 4 in the EDF-F, 7 in the EDF-S, and 9 in the EDF-N. They are listed in Table C.1. We estimated the spectroscopic cluster redshifts as the average of the redshifts of the concordant galaxies. For one cluster in EDF-N, we identify two groups of galaxies at different mean z, suggesting that this detections might be partly the result of overlapping structures along the line of sight.

Table A.2. Most reliable PZWav and AMICO-detected clusters at redshifts $z \geq 1.5$

NAME	ID	$\mathrm{RA_{PZWav}}$ (degrees)	$\mathrm{Dec_{PZWav}}$ (degrees)	$\mathrm{RA_{AMICO}}$ (degrees)	$\mathrm{Dec_{AMICO}}$ (degrees)	$z_{\rm PZWav}$	$z_{\rm AMICO}$	$\mathrm{SNR_{PZWav}}$	$\mathrm{SNR_{AMICO}}$	$\lambda_{\rm Pmem}$
EUCL-Q1-CL J180351.79+674957.7	EUCL-Q1-HzCL-0	270.9647	67.8332	270.9669	67.8322	1.56	1.56	22.91	34.18	44.15±1.60
EUCL-Q1-CL J180720.52+653940.4	EUCL-Q1-HzCL-1	271.8386	65.6585	271.8324	65.6640	1.97	1.98	21.01	34.07	10.39±2.24
EUCL-Q1-CL J175448.16+654559.8	EUCL-Q1-HzCL-2	268.7050	65.7638	268.6963	65.7694	1.55	1.55	14.17	23.50	17.40±1.02
EUCL-Q1-CL J034654.61−480825.0	EUCL-Q1-HzCL-3	56.7254	−48.1447	56.7297	−48.1359	1.70	1.74	13.32	17.41	34.83±1.25
EUCL-Q1-CL J181953.75+651241.1	EUCL-Q1-HzCL-4	274.9701	65.2106	274.9779	65.2122	1.77	1.80	11.93	19.57	17.33±1.37
EUCL-Q1-CL J181349.12+674651.3	EUCL-Q1-HzCL-5	273.4570	67.7727	273.4523	67.7891	1.56	1.56	10.80	18.27	33.25±1.19
EUCL-Q1-CL J180347.27+640019.4	EUCL-Q1-HzCL-6	270.9477	64.0089	270.9462	64.0019	1.95	1.96	10.24	25.00	7.74±1.52
EUCL-Q1-CL J034533.23−500806.7	EUCL-Q1-HzCL-7	56.3879	−50.1344	56.3889	−50.1360	1.69	1.77	9.78	20.01	13.92±1.24
EUCL-Q1-CL J033056.82−284246.3	EUCL-Q1-HzCL-8	52.7357	−28.7109	52.7378	−28.7148	1.47	1.52	9.59	17.63	17.68±1.51
EUCL-Q1-CL J041546.25−495532.5	EUCL-Q1-HzCL-9	63.9408	−49.9269	63.9447	−49.9244	1.59	1.57	9.45	16.89	12.15±1.46
EUCL-Q1-CL J033730.18−283827.6	EUCL-Q1-HzCL-10	54.3729	−28.6438	54.3786	−28.6382	1.51	1.49	9.17	16.39	12.05±1.88
EUCL-Q1-CL J040832.33−473418.8	EUCL-Q1-HzCL-11	62.1376	−47.5722	62.1318	−47.5716	1.79	1.81	8.89	17.58	8.51±1.51
EUCL-Q1-CL J033722.21−283404.8	EUCL-Q1-HzCL-12	54.3415	−28.5675	54.3435	−28.5685	1.70	1.70	8.82	22.31	8.97±1.48
EUCL-Q1-CL J175433.97+674611.6	EUCL-Q1-HzCL-13	268.6438	67.7704	268.6393	67.7694	1.55	1.54	8.73	21.09	12.90±0.36
EUCL-Q1-CL J034923.66−481352.5	EUCL-Q1-HzCL-14	57.3443	−48.2336	57.3529	−48.2289	1.85	1.89	8.59	16.40	9.94±0.70

Table B.1. Cluster match breakdown in EDF-S

Cluster sample	Matches with *Euclid* Q1	Unique matches with *Euclid* Q1
MCXC-II	0	0
MCSZ	15	5
ComPRASS	3	0
eROSITA	39	6
MCCD	2	0
LC^2	0	0
Abell	3	0
DES Y1 RM	71	41
In two catalogues		23
In three catalogues		6
In four catalogues		3
In five catalogues		1
In six catalogues		0
Unmatched		106
Total		191

Notes. No additional match from NED, 40 additional matches from MaDCoWS2, and 51 additional matches from WH24.

Table B.2. Cluster match breakdown in EDF-F

Cluster sample	Matches with *Euclid* Q1	Unique matches with *Euclid* Q1
MCXC-II	3	1
MCSZ	3	1
ComPRASS	0	0
eROSITA	10	3
MCCD	0	0
LC^2	0	0
Abell	1	0
DES Y1 RM	13	9
In two catalogues		5
In three catalogues		2
In four catalogues		0
Unmatched		77
Total		98

Notes. 20 additional matches from NED, 23 additional matches from MaDCoWS2, and 29 additional matches from WH24.

Table B.3. Cluster match breakdown in EDF-N

Cluster sample	Matches with *Euclid* Q1	Unique matches with *Euclid* Q1
MCXC-II	4	3
MCSZ	0	0
ComPRASS	0	0
eROSITA	0	0
MCCD	0	0
LC^2	0	0
Abell	1	0
DES Y1 RM	0	0
In two catalogues		1
In three catalogues		0
Unmatched		133
Total		137

Notes. 29 additional matches from NED, No additional match from MaDCoWS2, and 7 additional matches from WH24.

Table C.1. Cluster candidates with concordant spec-z galaxies

Candidate id.	N_c	$\bar{z}$ (spectroscopic)	z_{DET} (PZWav)	z_{DET} (AMICO)
EUCL-Q1-CL-21	4	1.0746 ± 0.0039	1.04	1.04
EUCL-Q1-CL-200	3	1.0931 ± 0.0054	1.12	1.13
EUCL-Q1-CL-211	3	0.9199 ± 0.0028	0.98	0.96
	4	0.9932 ± 0.0016		
EUCL-Q1-CL-415	2	0.9644 ± 0.0048	1.04	1.04
EUCL-Q1-CL-128	2	0.9395 ± 0.0018	0.92	0.89
EUCL-Q1-CL-231	2	0.9782 ± 0.0001	0.95	0.92
EUCL-Q1-CL-248	2	1.0162 ± 0.0035	0.95	0.98
EUCL-Q1-CL-277	3	1.2610 ± 0.0003	1.26	1.26
EUCL-Q1-CL-285	3	1.3223 ± 0.0048	1.21	1.26
EUCL-Q1-CL-333	3	0.9464 ± 0.0020	1.04	1.02
EUCL-Q1-CL-403	3	1.0079 ± 0.0031	0.94	0.93
EUCL-Q1-CL-288	2	0.9777 ± 0.0011	0.93	0.99
EUCL-Q1-CL-154	4	1.0439 ± 0.0006	1.00	0.96
EUCL-Q1-CL-286	3	1.1001 ± 0.0007	1.04	1.05
EUCL-Q1-CL-45	2	1.1966 ± 0.0011	1.18	1.16
EUCL-Q1-CL-346	2	1.2113 ± 0.0009	1.32	1.32
EUCL-Q1-CL-351	3	1.3512 ± 0.0012	1.37	1.38
EUCL-Q1-CL-87	2	1.3667 ± 0.0013	1.38	1.37
EUCL-Q1-CL-247	2	1.5068 ± 0.0014	1.45	1.46
EUCL-Q1-CL-424	3	1.5162 ± 0.0010	1.45	1.43

Notes. N_c is the number of galaxies with concordant spectroscopic redshifts as determined from *Euclid* spectra. Candidate EUCL-Q1-CL-211 has two groups of three and four galaxies with concordant z's along the line of sight.